In vivo sarcomere length measurement and total body irradiation

A thesis submitted for the Degree of
Master of Science in Physics

Peter Love

Department of Physics and Astronomy
University of Canterbury
Christchurch, New Zealand

1996

Contents

Figures

Tables

Abstract

This thesis contains work carried out in two separate fields of medical physics. Firstly, an instrument is described which enable orthopaedic surgeons to measure the *in vivo* sarcomere length in muscle fibre. The technique relies on the diffraction of laser light as it passes through the periodic structure of striated muscle. The resulting instrument is a modification of one described by other workers. Various refinements to the instrument were carried out and tested during several tendon-transfer operations. A precision of 3% in the sarcomere length may be achieved which is adequate for the surgeons needs.

Secondly, simulations and experiments were performed to investigate an arcing Total Body Irradiation technique to be used in radiotherapy. The technique was first proposed by workers at Christchurch Hospital and this work continues that study. Computer code was written to simulate the treatment using Monte Carlo methods for radiation transport. Various characteristics of the treatment were examined such as dose rates, dose uniformity and dose compensation. These properties must be known if the treatment is to be implemented in a clinical situation. An anthropomorphic model was used which demonstrates the dose uniformity achievable with this method.

Chapter 1

Introduction

Work has been carried out in two fields of medical physics of interest to local hospitals. The first project is presented in chapter 2 and describes the development of a specialized instrument for use in orthopaedic surgery. The second project is presented in chapters 3, 4 and 5 and describes the investigation into a new radiotherapy treatment planned for use at the Oncology Service at Christchurch Hospital. Concluding remarks are made in chapter 6 regarding both projects.

Tetraplegia is caused by broken necks injuring the spinal cord. Depending on the location of the injury, some shoulder movement is still possible. These people may benefit from surgical techniques that restore useful movement to the arms and hands. A procedure which achieves this is a deltoid-triceps tendon transfer where the tendon from a patients shin is removed and placed in the upper arm. The added mobility is achieved by attaching one end of the tendon to the still functional posterior-deltoid and the other end to the paralysed and wasted tricep. This requires the patient to undergo intensive physiotherapy but eventually the muscle may be trained to operate in its new location.

Muscle fibres consist of microscopic structures called sarcomeres which are the basic working unit of the muscle. During normal movement the length of the sarcomere changes in a way which depends on the force applied and the length of the muscle. Surgical transfer may alter this relationship and muscle strength may be compromised post-surgically due to the altered sarcomere length operating range. Adjustment of the muscle length during tendon transfers presents a problem for surgeons. Guidelines for adjusting the muscle length are based on the total muscle excursion and the passive tension felt during surgery. Since the muscle is usually under tourniquet control and the patient anaesthetized, these techniques are a poor indication of the muscle behaviour under active tension. The surgeon evaluates the correct tension using their personal experience. A more effective approach is to adjust the sarcomere

length to the value which gives the maximum tension when the muscle is in its functional position (Fleeter *et al*, 1985).

The large number of sarcomeres in muscle fibre are regularly arranged in a periodic structure. When illuminated with monochromatic light a diffraction pattern is observed consisting of a series of parallel lines (Sandow, 1936). This pattern may be used to measure sarcomere length during the operation. An instrument was developed capable of measuring *in vivo* sarcomere length. It works by using a prism to deflect a He-Ne laser beam through a bundle of muscle fibre then displays the characteristic diffraction pattern. At present, the instrument is capable of measuring sarcomere length to a precision of better than 5% which is adequate for the surgeons needs.

The second project investigates problems surrounding a proposed technique to deliver total body radiation. Acute myelogenous leukaemia is a disease which affects people of all ages. The disease is treated with chemotherapy, red cell transfusions and bone marrow transplants. In the latter treatment a combination of the drug cyclophosphamide and total body irradiation (TBI) is used to ablate the patients bone marrow, prior to infusing healthy marrow from a histocompatible sibling. The main requirement for any TBI treatment is a uniform dose distribution throughout the patient volume (Glascow and Mill, 1980). Megavoltage ionizing raddiation is used and usually requires a large field size ($50 \times 200\,\mathrm{cm}^2$), which poses a problem because most therapy machines are not capable of this or the room design prevents the source-to-skin distance (SSD) required. Some cases require a SSD up to 4 m long (Kim *et al*, 1980).

Centres manage to improvise TBI with complicated techniques such as using horizontal beams with the patient lying on their side, or sometimes even curled up into a small space and using custom-made compensators. A serious problem with these techniques is the increased dose to the lung of up to 24% when assuming a uniform density patient (Van Dyk *et al*, 1980). Lung compensation is usually required but it is used with difficulty because of the problems placing the custom-made shield accurately.

Pla *et al* (1983) developed a sweeping beam technique where the head of a 4 MV linear accelerator was rotated about the source. The patient lies beneath the beam in both prone and supine positions while the beam sweeps over them. With a SSD of 190 cm, the variation in mid-line dose is less than $\pm 5\%$. Bolus is placed around the head and legs to provide scatter and lead shields protect the lungs. This is a successful technique for centres with swivel mounted head

units.

An opposite approach used by Quast (1985) uses a stationary Cobalt-60 source but translates the patient through the beam on a special couch. The dose distribution in this case is controlled by the speed with which the couch moves. This technique produces a $\pm 7\%$ homogeneity with long treatment times (3-4 hours) and requires lung shielding.

At Christchurch Hospital the delivery of TBI is currently performed with an open Cobalt-60 machine with the patient lying on a low couch with a SAD of 170 cm. This allows the beam divergence to provide the large field required. After the initial dose is delivered a boost dose to the head and feet will usually be required, depending on the dose measurements taken during the treatment. This method has the major disadvantage that the Cobalt unit is temporarily modified making it unusable for other treatments.

A new technique to deliver the dose with an isocentric linear accelerator is the focus of this project. The method uses a sweeping beam similar to Pla *et al* (1983) but has a very short vertical SSD of 150 cm. The beam rotates about the isocentre which is 100 cm from the source, requiring the gantry to rotate over a large angular range. The short SSD enables the patient to lie on the existing treatment couch. This makes preparations quick and simple and is comfortable for the patient. Compensating in areas such as the feet and head is performed by modulating the linear accelerator output as it sweeps over the patient. With a small field size, detailed variations in the dose profile may be achieved but must be weighed against the treatment time required. The biggest advantage of this arc-TBI technique is that the machine requires no modification and the treatment may be integrated amongst the other work of the clinic.

The work presented here is a simulation of the process using Monte Carlo methods to transport radiation through a phantom. It was originally envisaged to take real measurements but that option required the linac software to modify the beam output. This software was not forthcoming from the manufacturers so the next best option was taken, namely simulating the experiments. This decision proved fruitful as various changes to the technique may be made easily and problems rectified before the tedious and time-consuming experiments are carried out.

Chapter 3 describes the arc-TBI technique in detail, giving results from initial experiments using an unmodified beam. The dose resolution for various field sizes is mentioned along with the expected treatment times required to

deliver a prescribed dose. Chapter 4 outlines the physics involved in transporting radiation and details features of the code TBIDOS written to mimic the arc-TBI method. An attempt to justify the Monte Carlo approach as opposed to simpler algorithms is included. The results of using TBIDOS are in chapter 5 culminating with an anthropomorphic treatment scenario.

Chapter 2

In vivo sarcomere length measurement

An operation frequently performed at Burwood Hospital is the deltoid-triceps tendon transfer which returns movement to the elbow of tetraplegics. This added motion enables the patient to perform tasks such as lifting and operating a wheelchair, restoring lost independence. The functionality of a muscle may change when its length is altered such as when the deltoid is surgically moved from its normal location. If the deltoid is stretched slightly before attaching the tendon, the optimal muscle length may be obtained leading to better recovery with less pain. The ideal amount of stretching is not known. To enable a proper study to be undertaken the amount of stretching needs to be quantified. This is done by measuring the sarcomere length within the muscle at pre- and post-transfer stages giving a percentage increase in length. As a first step, an instrument capable of measuring the sarcomere length *in vivo* was built and then tested during these tendon-transfer operations.

2.1 Muscle structure

The three major types of muscle in vertebrates are *skeletal*, *cardiac* and *smooth*. Each has a specific role to play. Skeletal muscle is capable of powerful contractions of 100 watts per kilogram but has a limited contraction range. Large movements are achieved by utilizing the lever action of the skeleton, giving this type of muscle its name. It is also called *voluntary muscle* because its movements are usually initiated consciously. Cardiac muscle (i.e. heart) is specialized to be fatigue resistant and only produces 3-5 watts per kilogram. Smooth muscle is generally controlled involuntarily by the autonomic nervous system and is widely spread throughout the body.

Skeletal and cardiac muscle are also referred to as *striated* muscle because of the appearance of cross-striations when viewed under a light microscope. Figure 2.1 shows the structure of skeletal muscle. The macroscopic bulk of the

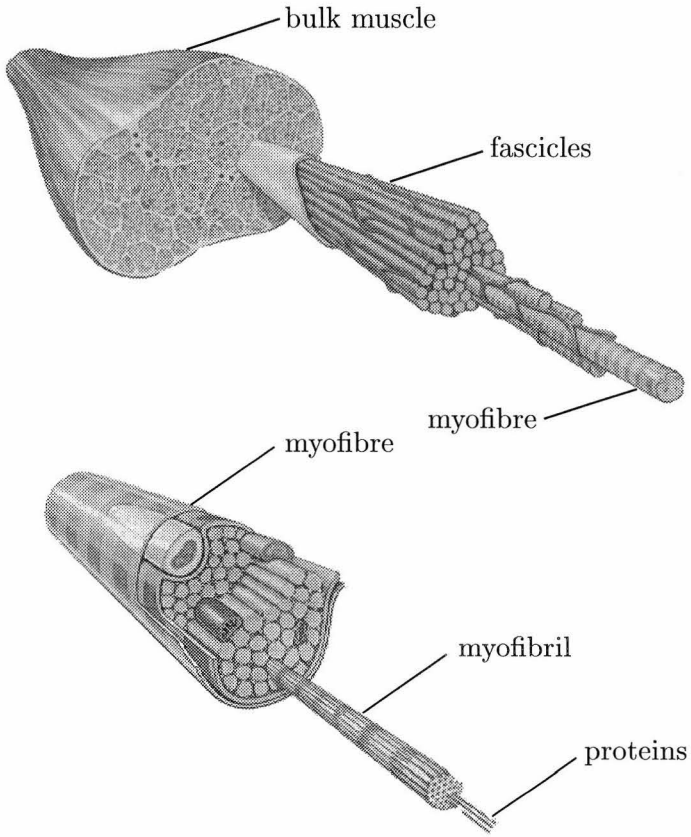

Figure 2.1: Various levels of muscle structure from the whole muscle and fasciculi (top), down to single myofibre and myofibrils (bottom). After Salmons (1995).

muscle is composed of *fascicles*, the strands visible to the naked eye when cutting into red meat or poultry. Each fascicle is composed of *fasciculi* which are bundles of muscle fibres or *myofibres* separated by the membrane perimysium. Each myofibre is 10-50 μm in diameter and 1-40 mm in length. Myofibres in turn consist of *myofibril* bundles surrounded by a plasma membrane called endomysium. Myofibrils are about 1 μm in diameter. Myofibrils are a long assembly of the contractile proteins actin and myosin which alternate along its length. Actin is a thin filament compared to the thicker myosin protein and this difference gives the alternate light and dark appearance of the myofibril shown in figure 2.2. The figure also shows how the thin actin merges with the

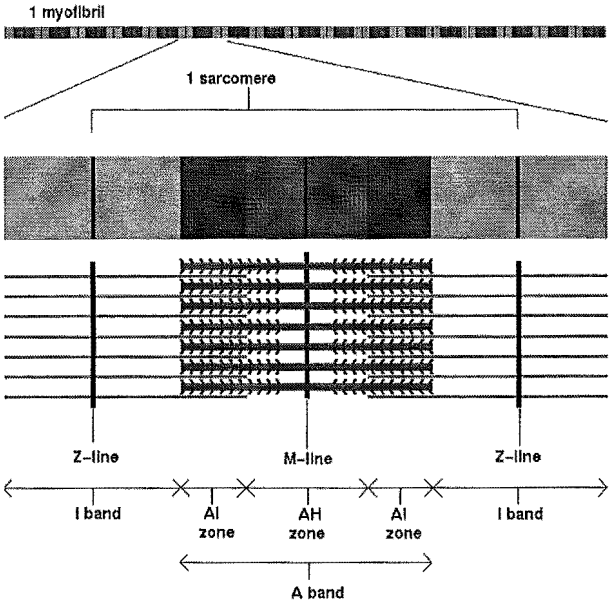

Figure 2.2: Contractile proteins actin (thin) and myosin (thick) form the structure of individual sarcomeres. Their different thickness cause the light and dark appearance of the myofibril. Muscle contraction occurs when the actin and myosin slide pass each other.

myosin to form the basic working unit of striated muscle, the *sarcomere*.

The contraction of muscle occurs due to the shortening of the sarcomere (Huxley and Niedergerke, 1954; Huxley and Hanson, 1954). The actin and myosin filaments retain their length but cause the sarcomere shortening, by sliding past one another, and powered by ATP molecules. Referring to figure 2.2, the width of the AI band increases at the expense of the AH zone, so that the total width of AI and AH (i.e. the length of a myosin thick filament) is invariant. As the length of the actin filaments is also constant, the increase in the width of AI is matched by a decrease in I and the sarcomere as a whole is shortened.

Figure 2.3 shows a light micrograph of the characteristic striated muscle caused by the precise alignment of sarcomere from different myofibril across the cell. This example shows well-ordered striations perpendicular to the myofibrils but more often they are skewed due to slight misalignment. The diffraction

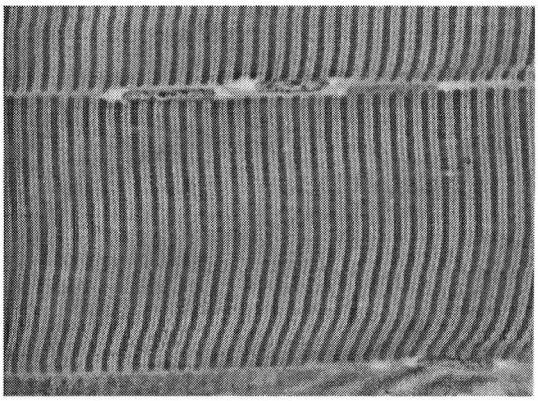

Figure 2.3: Light micrograph of skeletal muscle showing the striations caused by alignment of sarcomere between myofibrils. A-bands, I-bands and Z-disks are clearly visible in this stained sample. The two horizontal lines mark the division between domains with different sarcomere length.

of monochromatic light by this periodic structure has been used for many decades (Sandow, 1936) to study the dynamic behaviour of skeletal muscle. Theories explaining the observed diffraction patterns in great detail have been formulated, some of which are mentioned below.

2.2 Muscle diffraction theory

The analysis of light diffracted by muscle fibre gives clues to the dynamic behaviour and mechanics of muscular activity. Interpreting these clues requires a theory capable of modelling the sarcomere precisely. Experimental setups studying muscle diffraction patterns usually consist of a monochromatic light source, lasers in recent cases, which illuminate muscle samples and record the diffraction pattern photographically or with electronic detectors.

A coupled-wave analysis of the wave equation describing light diffraction by muscle fibre was performed by Sidick *et al* (1992) and is capable of analysing remarkable detail in the sarcomere structure. The Thornhill model (Thornhill *et al*, 1991) used in this theory is shown in figure 2.4 and represents the varying refractive index within the sarcomere unit. This model is the most sophisticated to date and demonstrates the extensive research undertaken to describe features of muscle diffraction patterns. The sarcomere length is given

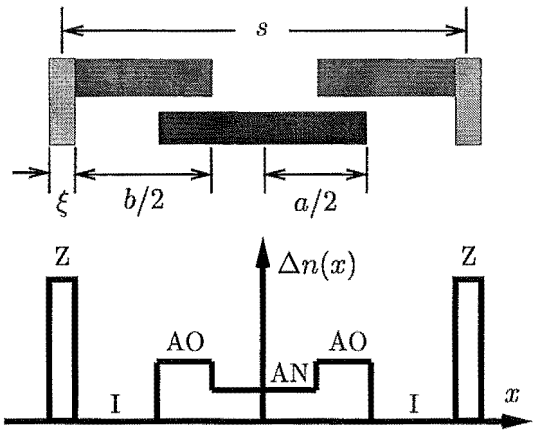

Figure 2.4: Sarcomere model used in the coupled-wave analysis (Sidick *et al*, 1992) of muscle fibre diffraction represents the most rigorous theory available. Seven regions with varying relative refractive index are modelled for every sarcomere unit. Sarcomere length is given by s.

by s with the A- and I-bands having length a and $b/2$ respectively. The thin Z-disc is also specified with length ξ. This model also successfully copes with the realistic situation of misaligned myofibrils. The striations may be straight, skewed or vary sinusoidally yet the coupled-wave approach accurately predicts the diffraction pattern in each case.

Other less rigorous theories such as those by Thornhill *et al* (1991) and Huxley (1990) predict nearly identical results as Sidick but this is due to the similar refraction indices present in the striated structure. The more elementary theories of Yeh *et al* (1980) and Rüdel and Zite-Ferenczy (1979) are able to predict the position of diffraction maxima with or without myofibril skew but lack the ability to explain the ratio of intensities between orders.

As a first approximation the regularly spaced light and dark striations of skeletal muscle, the I- and A-bands, behave like a simple one-dimensional diffraction grating. It has been shown on whole muscle fibres (Sandow, 1936) and on single fibres (Buchthal and Knappeis, 1940) that the diffraction line spacings satisfy the grating equation

$$n\lambda = d\sin\theta \tag{2.1}$$

where

$$n = \text{diffraction order},$$
$$\lambda = \text{light source wavelength},$$
$$d = \text{sarcomere length},$$
$$\theta = \text{diffraction angle}.$$

This simple relation is used frequently to determine the average sarcomere length both by others and throughout this work.

2.3 Preliminary investigation

A series of tests were performed to observe the pattern and evaluate requirements for an *in vivo* sarcomere length measuring device. The validity of using the grating equation was confirmed by measuring the sarcomere length under a light microscope and comparing the value with that obtained using the diffraction technique.

A small sample of beef muscle fibre, approximately 4 mm long and 1 mm diameter, was dissected free from a piece of shank. Shank was selected because large distinct fascicles are present and easily separated. The sample was immersed in a weak saline solution to prevent the muscle deteriorating and then mounted on a slide under a cover slip. The sample was then observed using a light microscope with a $\times 500$ magnification and striations similar to figure 2.3 were seen. The average sarcomere length was obtained by measuring the length of 20 bands using the microscope scale with appropriate multiplier.

The same slide and sample was then mounted on an optical bench and illuminated with a He-Ne laser of wavelength $\lambda = 633$ nm (Melles-Griot, model 05-LHP-111). The resulting diffraction pattern was projected onto a screen at a distance of $h = 150$ mm from the slide. The distance x_1 from the zeroth order to the first order was measured using calipers and repeated for the second order. With this setup the mean sarcomere length may be obtained using

$$d = \frac{n \times 0.633}{\sin(\tan^{-1} x_n/150)} \ (\mu\text{m}). \tag{2.2}$$

Mean sarcomere lengths were calculated from order spacing measurements using equation 2.2 for six muscle samples, each crudely stretched a different

amount. The precision of the measurement was within ±0.5 mm giving a sarcomere length precision of ±0.05 μm when using the first order. The microscope measurements had a precision of ±0.05 μm and all the values agreed with the diffraction method within this uncertainty. High precision measurements have confirmed this agreement time and again such as those performed by Sandow (1936), Kawai and Kuntz (1973), Paolini *et al* (1976), Rüdel and Zite-Ferenczy (1979), Yeh *et al* (1980) and Baskin *et al* (1981). A resolution of 0.008 μm was reported by Paolini *et al* by using a camera imaging system to measure the distance between diffraction peaks. These agreed with their microscope readings which were accurate to ±0.018 μm, a precision based on standard deviation calculations after counting 200 striations. This investigation and the results of others demonstrate the reliability of the grating equation to predict the average sarcomere length.

During these trials it was obvious that the quality of the diffraction pattern depends strongly on the muscle sample. Initially there was great difficulty obtaining a recognizable pattern due to a number of reasons. Firstly the thickness of the bundle is important with thick samples simply being too opaque. With beef samples clear results were obtained by teasing the fibre into many small strands less 0.2 mm thick. The age of the sample is another factor. Most refrigerated pieces were not usable except when fibres from the interior of the bulk muscle were chosen. All samples tended to dry out within a 10 minute period with the pattern decaying over this time. A biopsy obtained during the first operation showed how fresh healthy tissue has far superior diffraction properties. Lines were very sharp and intense with this sample. The inhomogeneous nature of muscle fibre was apparent when viewed under a microscope with striation quality changing from each location. This is apparent when trying to obtain diffraction patterns, some locations produce excellent results with others producing mediocre or no results. The physiological reason behind this is unclear but may be due to over-stretching or damage during preparation. The best bundle thickness to use is about 1-3 mm, any less is far too fragile, even though Lieber *et al* (1984) states small fibre bundles and large laser beam widths are optimal.

2.4 Instrumentation

The objective of this work was to produce an instrument capable of measuring the sarcomere length *in vivo*. Lieber and Baskin (1985) have described

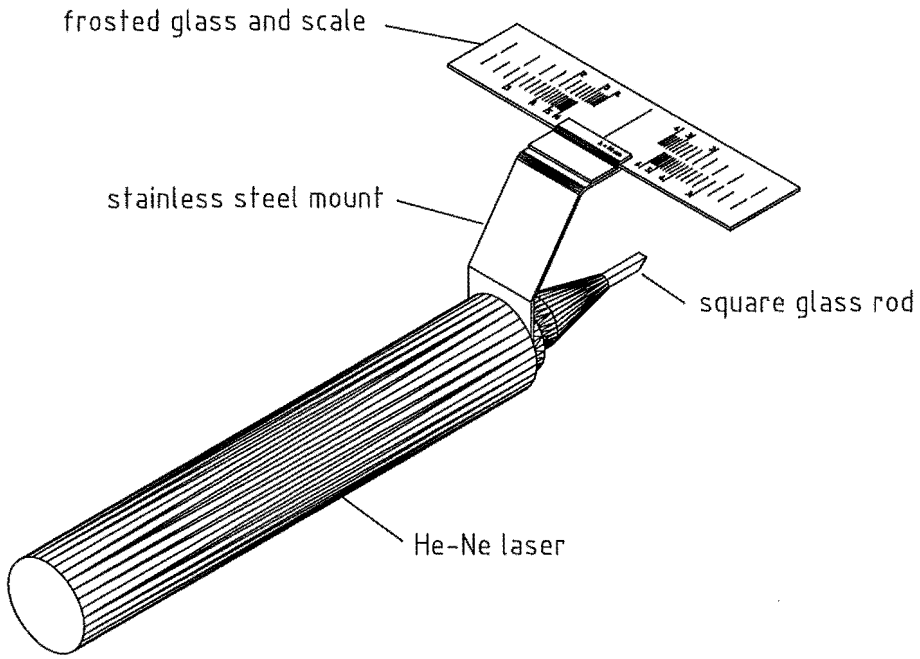

Figure 2.5: Instrument used to measure the sarcomere length during an operation. The glass screen scale is calibrated to give a direct sarcomere length reading in μm.

an instrument capable of doing this. The instrument design allows a He-Ne laser beam to pass down a tube where a prism is used to redirect the beam. The prism reflects the beam 90° enabling it to pass through a small bundle of muscle fibre which is positioned over the top surface of the prism. The diffraction pattern produced is projected onto a screen enabling the surgeon to observe the pattern from above.

Their instrument served as the basis for a similar model built for this thesis. Various modifications and improvements were made after several trials in theatre. Firstly, a diode laser was trialed as these are much smaller and cheaper than a He-Ne gas laser but it was unsuccessful at producing a clear diffraction pattern. A pattern was obtained when shining the light directly at the muscle in controlled conditions, but when passing the light through optics during an operation, the combination of a diode's low intensity and short coherence length failed to produce a pattern. The screen used was coarsely ground which merely compounded the problems. The following versions used a He-Ne gas laser. The possibility of using a diode laser still exists but would

require one with higher beam quality combined with professionally prepared optics.

A new screen was made from a sheet of photographic glass ground with 800-grade silica carbide (The Carborundum Company Ltd, England) until it became semi-opaque. This fine powder was used rather than the coarser grit used previously because the pattern was much clearer when projected onto the screen. A scale was printed (Kelly Engravers Glassprint Ltd, Christchurch) on the frosted side of the screen calibrated to read the sarcomere length in micrometres. Two scales are used, one each for the first and second orders and depend on the muscle-screen distance. The first order scale is more precise for shorter sarcomere length measurements and the second order scale used with stretched muscle with its longer sarcomeres. A glass rod was used instead of a standard right-angled prism for simplicity as this does away with the need to bond a prism to the mount. The instrument must be sterilized in an auto-clave which reaches temperatures of 135°C so avoiding the use of chemical bonds is preferred. The top face on the circular rod proved difficult to polish and the cross-section produced by making a flat face on a curved surface caused an unacceptable amount of light loss. The interference of this scattered light with the diffracted beam degrades the pattern quality. Miscellaneous scattered light, from the muscle fibre and elsewhere, is also responsible for interference effects such as those observed by Burton and Huxley (1995) which caused an incorrect interpretation of dynamic muscle behaviour (Altringham *et al*, 1984). A half-dozen rods were polished, some with a bulbous end to avoid the cross-section difficulties. Grinding facilities in the department meant the final product was not of the highest quality and the time spent perfecting polishing techniques was not justified. In the end square rods were commissioned which improved beam quality immensely because of the fine polish achievable.

The 45° face was coated with aluminium to reflect all the light through the muscle. Without the coating, the surface becomes soiled with blood and other fluids allowing light to escape the total internal reflection surface and making the diffraction pattern difficult to see. Unfortunately, aluminium does not survive the auto-clave process so a more durable metal will be required. To increase the life of the metal coating the auto-clave should be avoided and gas-sterilization should be used for the glass rod.

A small 5 mW He-Ne laser was purchased from Melles-Griot special range (model 05-LHP-211). This has a small 32 mm diameter easily grasped during an operation. It is still mains-powered requiring plastic coverings around the

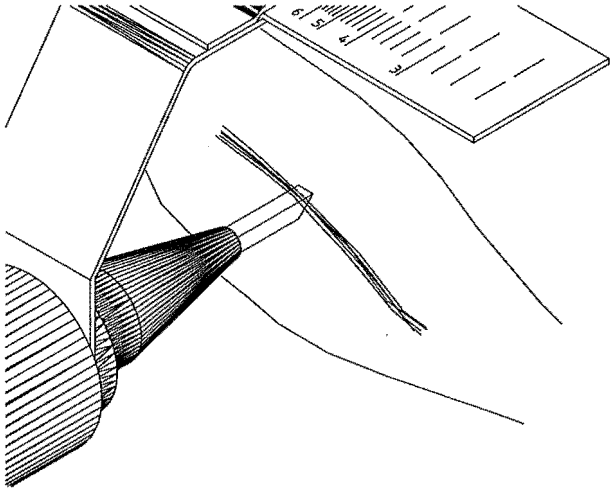

Figure 2.6: Detail of muscle placement over the glass rod. A small bundle of muscle 1-3 mm in diameter is separated from the muscle bulk, but leaving the ends attached. Care must be taken not to stretch the sample being measured.

cord to maintain sterility. This is where a battery-powered diode laser would be more ergonomic.

2.5 Performance

Several deltoid-tricep tendon transfer operations were attended and various versions of the instrument were trialed. As mentioned, the surgeon desires to measure the degree of stretching during the operation at pre- and post-transfer stages. In order to test the consistency of results the measurements were repeated several times with the muscle in a relaxed position. A bundle of fibres approximately 1 mm in diameter was separated from the muscle bulk for a length of 30 mm whilst leaving the ends attached (figure 2.6). Care was taken not to apply any tension to this strand which would cause unwanted sarcomere stretching. The instrument was placed under the sample and positioned until a clear diffraction pattern was obtained. In the early versions the distance between orders -1 and 1 was measured using calipers then a lookup table was used to convert this distance to a sarcomere length. The precision obtained depends on the quality of the diffraction pattern. For good patterns the width

of individual lines is approximately 0.5 mm, as measured with a ruler, and for the lowest quality patterns which remain useful, this width increases to 3 mm. A change in x of $\Delta x = 0.5$ mm will give a change in the sarcomere length d of $\Delta d = 0.1\,\mu$m, a significant fraction of the $\simeq 3\,\mu$m length being measured. Values of $2.5 \pm 0.1\,\mu$m were obtained by averaging several measurements from the first and second orders. The detached muscle was then stretched by an amount considered excessive and further measurements were obtained yielding a sarcomere length of $3.5 \pm 0.1\,\mu$m. This stretching was greater than the natural stretching caused by limb movement and produced a sarcomere length increase of $40 \pm 5\%$.

The precision of the instrument may be improved by measuring x more accurately by making the sample-screen distance h larger. This extra precision is offset somewhat by the natural range of sarcomere length present in a length of muscle (Kawai and Kuntz, 1973). Light micrographs clearly show that muscle fibre is not homogeneous, but is organized into many domains. Each domain is distinguished by having different sarcomere lengths and tilt of striation. When the laser beam samples sarcomere from different domains, the length variation between the domains (up to 5%) causes the line width to increase. Also, angle of striation tilt means the diffraction pattern observed is due to a few domains at that particular location. This should be kept in mind and either take many averages along the muscle or keep the instrument in one place to measure the relative change at that location.

The sarcomere length for the deltoid muscle had a typical range of 2.5-4.0 μm compared to the 0.1 μm conservative precision of the instrument. This provides sufficient resolution to perform meaningful experiments when stretching the muscle.

Chapter 3

Arcing total body irradiation

Total body irradiation (TBI) is used widely to treat certain types of disease. The techniques used to deliver dose to the entire body vary greatly at different institutions, and is highly dependent upon the available equipment. Some of these methods are described in chapter 1. Large hospitals have dedicated facilities set up to deliver TBI exclusively. At smaller hospitals there are fewer patients to treat with TBI and existing equipment must be modified to supply the dose. A new technique to deliver this dose with a linear accelerator has been proposed and is investigated further. This chapter introduces the technique and details the initial work done for this thesis. Firstly, measurements were made to compare with predicted values, ensuring the validity of initial assumptions. The detail of dose variation along the patient is dependent on treatment time. These are important parameters in the clinical environment, and are investigated below. The dose uniformity is demonstrated in chapter 5 using the methods described in chapter 4. The treatment will be implemented on a linac as another routine option. This will occur after the technique has been demonstrated successfully.

3.1 Initial measurements

The proposed arcing-TBI technique involves rotating the linac gantry while the beam is on to produce a sweeping fan-shaped beam. The patient's umbilicus is positioned a distance $f - f_0 = 50\,\text{cm}$ below the machine's isocentre with the couch perpendicular to the axis of rotation, enabling the beam to sweep across the entire length of the patient. The location along the patient is specified by l as shown in figure 3.1. As the gantry rotates through a range of angles θ, the linac electron gun current may be modulated to control the photon beam intensity. Ideally, this modulation should produce a uniform dose profile throughout the patient volume or any other profile prescribed for the

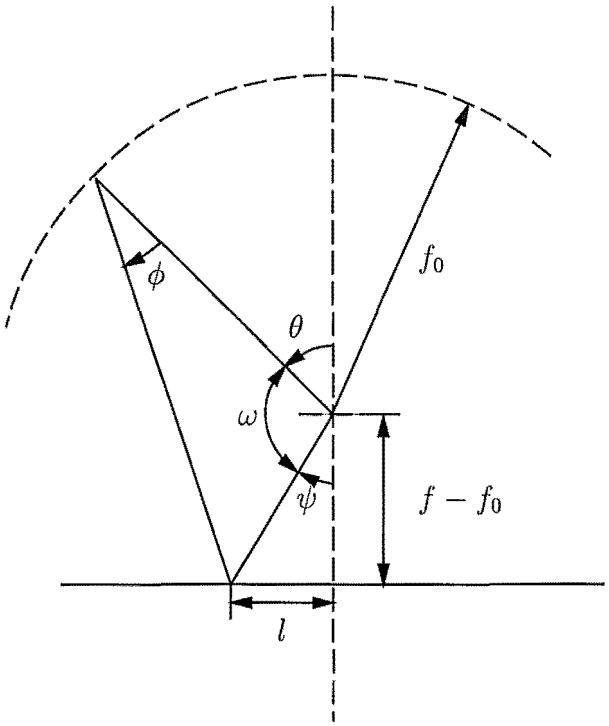

Figure 3.1: Definition of angles and lengths for the arc-TBI geometry. The source is located on the dashed arc at an angle θ and a distance $f_0 = 100\,\text{cm}$ from the isocentre. The dose reference point at the umbilicus ($l = 0\,\text{cm}$) is a distance f vertically below the source when $\theta = 0°$. Photons travel at an angle ϕ from the source with a spread depending on the beam width $\Delta\phi$.

treatment.

A feasibility study has already been carried out (Hugtenburg *et al*, 1994) with a vertical source-to-surface distance of $f = 200\,\text{cm}$. The 2100c linac output was controlled via a PC connected to the accelerator. The PC monitored the gantry angle and used a lookup table to alter the dose per degree. The resulting measurements of the surface dose in a regular phantom confirmed a flat dose profile within the required $\pm 5\%$.

With assistance from Richard Hugtenburg, a Ph.D. candidate, an experiment was carried out to confirm the predicted dose. Initial measurements were made in a homogeneous phantom with a constant beam output. The control

software which enables a sweeping beam was not available so depth doses were measured with the beam at discrete angles θ. A Clinac 600C (Varian Associates) linear accelerator was used to produce a 6 MV x-ray beam. The dose was measured with a diode in a water tank of dimension $60 \times 60 \times 60\,\text{cm}^3$. The experimental setup had the water tank resting on a low couch such that the water surface was 50 cm below the isocentre giving $f = 150\,\text{cm}$. This shorter distance would allow a patient to remain on the existing treatment couch. Since this couch can not move lower, a temporary couch would be needed when using larger source-to-patient distances, detracting from the techniques advantages. Depth doses for angles of $\theta = 0°$, 20°, 40°, 50°, 60° and 70° with a 10 cm × 10 cm field were recorded. The tank was located at such a position so the field entered the top surface. At high angles this meant the lower edge of the beam was very close to the top edge of the water tank. At $\theta = 70°$ it was not possible to fit the beam on the top surface and the lower edge entered the side of the tank which may decrease the dose due to a smaller scattering volume. The normalization point for each depth dose was chosen to be the point of maximum dose D_{max}. For a 6 MV beam D_{max} is at a depth of 15 mm along the path of the beam.

The RFA-300 computer was used to control the position of the diode and programed to take measurements along the beam axis for a length of about 30 cm. The effect of ionizing radiation on the diode p-n junction produces a current proportional to the exposure (Johns and Cunningham, 1983) enabling the relative dose at each angle to be compared. With a constant dose delivered (100 MU) a charge integration was made at the normalization point of each beam. The data were recorded and listed in table 3.1 and compared to an inverse square fall-off in figure 3.2. The dashed line is the inverse square fall-off and the solid line is a fit of the inverse square fall-off plus a linear component. It is thought the difference between the data and the inverse square relation is due to the higher dose at small angles of incidence from contaminating electrons. This is compared to the absence of these electrons at the extremities since they are attenuated through a larger volume of air. The close fit of the modified inverse square fall-off to the measured data indicates that compensating for this fall-off should give a uniform dose profile. These results agree with Hugtenburg *et al* where they used $f = 200\,\text{cm}$ as opposed to $f = 150\,\text{cm}$ used here. Using $f = 150\,\text{cm}$ allows the existing treatment couch to be used but gives a more extreme dose profile. This larger change in the dose between the umbilicus and feet simply means the output modulation will

θ (°)	Position l (cm)	Integrated charge (nC)	Relative dose
0	0.0	57.3	1.00
20	18.2	54.6	0.95
40	42.0	45.9	0.80
50	59.6	39.3	0.69
60	86.6	30.6	0.53
70	137.4	19.7	0.34

Table 3.1: Relative dose at $D_{\max}$ for the measurements at different gantry angles θ with $f = 150\,\text{cm}$. The integrated charge is for 100 MU measured at $D_{\max}$.

need to change faster as the beam passes over the patient.

3.2 Dose resolution

Using large beam widths gives a higher dose rate and shorter treatment times compared to using narrow beams. The drawback is the loss of resolution and the dose profile is only permitted to vary slowly over the length of the patient. Dose resolution is a measure of length along the patient where the dose delivered may ddiffer from a neighbouring element of length. A better resolution means a smaller section of a patient may recieve specified dose. This allows the dose prescription to be better taylored to the patient and helps reduce the dose to sensitive organs such as the lung. In order to find the largest usable field size (and shortest treatment time) for a required resolution, the resolution for various beam widths $\Delta\phi$ is investigated.

The expected surface dose profile $D(l)$ is the product of the linac output function $O(\theta)$ and uncompensated dose profile $S(\theta, l)$ convolved with the beam profile $B(\theta)$,

$$D(l) = O(\theta)S(\theta, l) * B(\theta). \tag{3.1}$$

Using the notation and geometry in figure 3.1 the uncompensated dose profile relative to the point $l = 0\,\text{cm}$ is given by

$$S(\theta, l) = \frac{f^2}{\sqrt{f_0^2 + l^2 + (f - f_0)^2 - 2f_0\sqrt{l^2 + (f - f_0)^2}\cos(\omega)}} \tag{3.2}$$

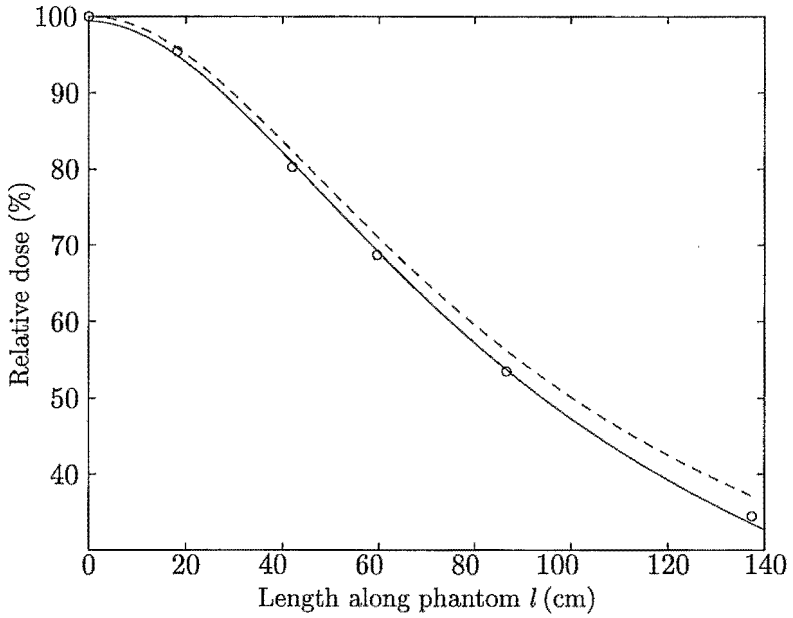

Figure 3.2: Relative dose between measured values (o) along the phantom and the inverse square fall-off (- -). The solid curve is the inverse square curve plus a linear fit of the residual values.

where $\omega = 180 - \theta - \psi$. This is the relative dose at any point l given the source location θ if only the inverse square fall-off is considered. A poor resolution is expected when using wide beams since any particular point at l receives dose from a range of θ. Neglecting treatment times, the ideal beam width is $\Delta\phi = 0°$ since each location would receive dose from a single source location θ and have the best resolution. To determine the resolution the output function $O(\theta)$ was zero for all values of θ greater than 40° and set to one for angles less than 40°. The dose $D(l)$ was calculated using equation 3.1 with beam widths $\Delta\phi = 0°$, 0.6°, 2.9°, 5.7°, 11.3° and 22.6° corresponding to field widths at the isocentre of 0 cm, 1 cm, 5 cm, 10 cm, 20 cm and 40 cm respectively. The resulting dose profiles are shown in figure 3.3. The rate of change in the profile gives an indication of the obtainable resolution. The resolution is defined as half the distance over which the dose differs from the ideal $\Delta\phi = 0°$ beam. For a wide beam the smoothing of the dose profile is due to the beam hitting a range of l which would otherwise be outside a narrow beam. Figure 3.3

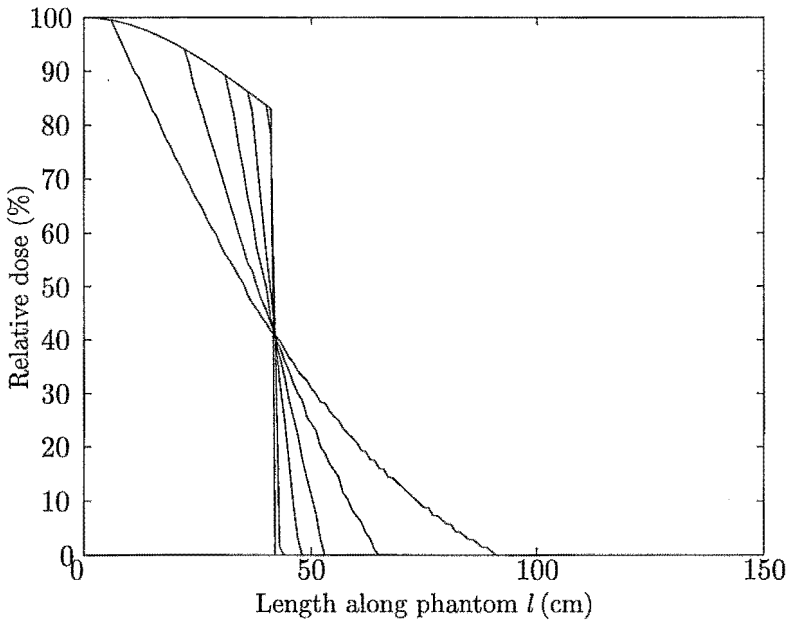

Figure 3.3: Dose profiles for various beam widths of $\Delta\phi = 0°$, 0.6°, 2.9°, 5.7°, 11.3° and 22.6° . The output function was set to zero at angles $\theta > 40°$ ($l > 42\,\text{cm}$). The sharp vertical line is when $\Delta\phi = 0°$ compared to the sloping curve $\Delta\phi = 22.6°$ which deposits dose up till $l = 90\,\text{cm}$.

shows how the narrow beam $\Delta\phi = 0.6°$ changes dose over 2 cm whereas the $\Delta\phi = 22.6°$ dose profile changes between 8 cm and 90 cm. Figure 3.4 is a plot of the resolution with beam width. From this graph the largest beam width for a required resolution can be obtained. Strictly these values only apply at this angle due to beam divergence. There would be better resolution near $l = 0\,\text{cm}$ and worse resolution at the phantom extremes. The angle $\theta = 40°$ was chosen because this is where the head would lie.

3.3 Treatment times

An important factor in determining the success of a new treatment is the time required to deliver the prescribed dose. With the treatment setup as a routine option on the linac, the preparation should be minimal and the actual beam-on time required needs to be estimated. This time may be estimated given the

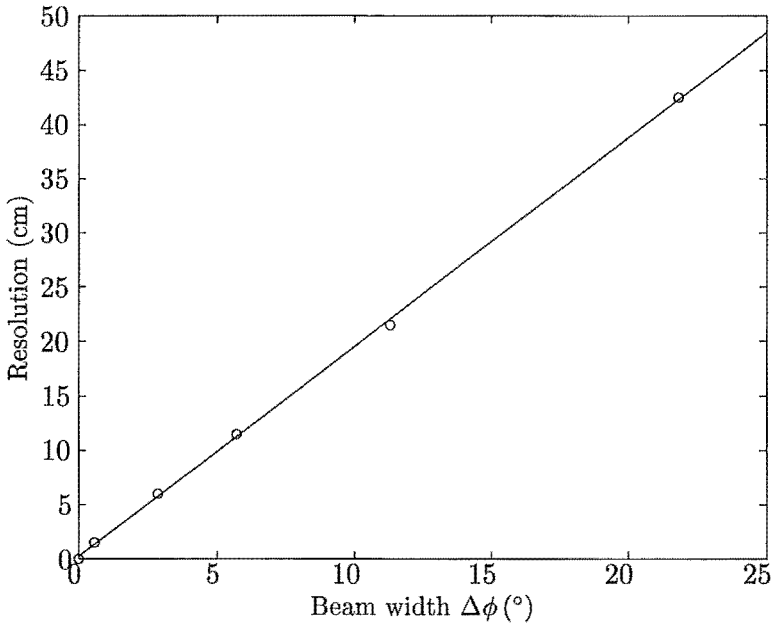

Figure 3.4: Resolution obtained for various beam widths at a moderate gantry angle $\theta = 40°$.

output dose rate and the total dose required. Dose per degree output by the machine is about $0.1\,\mathrm{Gy\,degree^{-1}}$ when using the linac's arcing mode. If high dose resolution is required like in the head and neck regions, a small beam width of $\Delta\phi = 5°$ would be used giving a dose at the reference point of about $D(0) = 0.5\,\mathrm{Gy}$ per treatment arc. Since the maximum dose rate is required at the extremes, the dose rate at the reference point will be reduced somewhat by a factor $D(l_{\max})$, taken to be 2.5 from figure 3.2. So we have

$$\begin{aligned} D_{\mathrm{ref}} &= \left(\frac{100\,\mathrm{cm}}{150\,\mathrm{cm}}\right)^2 \frac{0.1\,\mathrm{Gy\,degree^{-1}}\,5°}{2.5} \\ &= 0.09\,\mathrm{Gy}. \end{aligned} \tag{3.3}$$

For a prone/supine treatment the dose is twice this value and at the mid-plane the dose is less by the factor 0.55 as read from the depth dose curves, giving

the dose for a dual treatment arc of

$$\begin{aligned} D_{\text{arc}} &= 2 \times 0.55 \times 0.09\,\text{Gy} \\ &= 0.10\,\text{Gy}. \end{aligned} \tag{3.4}$$

At Christchurch Hospital 9 dose fractions of 1.33 Gy each are given for a total dose of 12 Gy. This means $1.33/0.10 = 13$ arcs per patient orientation is needed at each session with this beam width. If poor dose resolution is tolerated, say 45 cm, a wide beam with $\Delta\phi = 20°$ may be used which needs only 3 arcs per patient orientation. With each arc taking only 30 seconds, the treatment can be completed very quickly. Another option is to use different beam widths during one treatment, delivering the majority of the the dose with a wide beam then the remaining dose to selective areas with a narrow beam.

This gives an approximate indication on how the beam width affects treatment times. When the linac control software is available, the gantry velocity can be adjusted to give faster treatments.

Chapter 4

Monte Carlo Arc-TBI simulation

Monte Carlo techniques to simulate radiation transport have been used for many decades. The methods were first implemented in the 1950's for the study of electron- and photon-initiated showers in lead (Wilson, 1952). The stochastic element in these calculations was obtained by using a 'wheel of chance', which consisted of a spinning motorized cylinder marked with the probabilities of different interactions. The selection was made by a Geiger counter which turned the motor off when it detected a cosmic-ray. This gave the required randomness but was extremely tedious when more than a few particle histories were to be followed. The technique has become popular in the field of medical physics due to the computer codes ETRAN (Electron TRANsport) (Seltzer, 1988) and EGS4 (Electron Gamma Shower, version 4) (Nelson *et al*, 1985). With computer speed increasing rapidly, Monte Carlo methods will soon be used for routine work.

Arc-TBI experiments to investigate the effect of various parameters were proposed but not undertaken due to the linac control software being unavailable. Without the software to modulate the output of the accelerator it was decided to simulate the treatment using the EGS4 code system. The resulting program, called TBIDOS, outputs a dose map of the irradiated phantom given various treatment parameters. This chapter gives an introduction to the EGS4 code system and outlines the parameters chosen for the TBIDOS code.

4.1 Monte Carlo vs photon algorithms

Monte Carlo techniques may be used for simulating radiation transport but tend to be very time consuming. The alternative is to use photon dose distribution algorithms like those used in commercial treatment planning (Astrahan *et al*, 1990). The advantage of using these algorithms is their speed.

The four main interactions involved when a beam of x-rays enter a medium

are Rayleigh scattering, the photo-electric effect, Compton scattering and pair production. These have a different probability of occurring which depends on the photon energy and the nature of the medium. Figure 4.1 shows the likelihood of these interactions occurring in the water model used by TBIDOS. It is clear the Compton process is most dominant for the energy range (0-6 MeV) used in TBIDOS. A Compton interaction consists of a photon colliding with a (free) electron and transferring some energy to it. During this collision the resulting trajectory of the electron may be straight forward, gaining maximum energy or at the other extreme the trajectory may be 90° and the electron receives almost no energy. Any angle in between is allowed. The energy imparted to the electron may be obtained by the Klein-Nishina formula (Jackson, 1975). From this formula we can get the probability of each energy transfer and this may be used to give the average energy imparted to an electron given the photon energy $h\nu$. The mean photon energy in a 6 MV beam is about 1.5 MeV so the mean energy transferred to an electron is 0.74 MeV (ICRU Report 35, 1984). This kinetic energy released during the interaction is called the kerma, an acronym for Kinetic Energy Released in the Medium. The high speed electron loses energy via excitation and ionization collisions within the medium and deposits energy over a distance which depends on its initial energy. For example, an electron with a kinetic energy of 0.74 MeV will transfer this energy over a 3 mm range in water. It may also lose energy by producing bremsstrahlung photons which carry the energy further afield. These bremsstrahlung photons and the initial scattered photon then move on to interact in a similar manner to the original.

Photon algorithms firstly calculate the kerma from primary photons interacting with the medium. At depth d in the media this is given by

$$\mathrm{K_p}(d) = \int_0^{E_{\max}} \Phi_\mathrm{p}(E,d) \left(\frac{\mu_\mathrm{k}(E)}{\rho}\right) dE \tag{4.1}$$

where $\Phi_\mathrm{p}(E,d)dE$ is the primary energy fluence at depth d, $E_{\max}$ is the maximum photon energy in the beam and $(\mu_\mathrm{k}(E)/\rho)$ is the mass energy-transfer coefficient. Calculating the dose in a medium requires knowledge of the dose due to kerma plus any bremsstrahlung production from secondary particles. Photon dose algorithms make many shortcuts such as only calculating the kerma and assume the recoil electron energy is deposited at the point of interaction. This is reasonable where charged particle equilibrium (CPE) exists but is not satisfactory in the buildup region or where there are tissue inhomo-

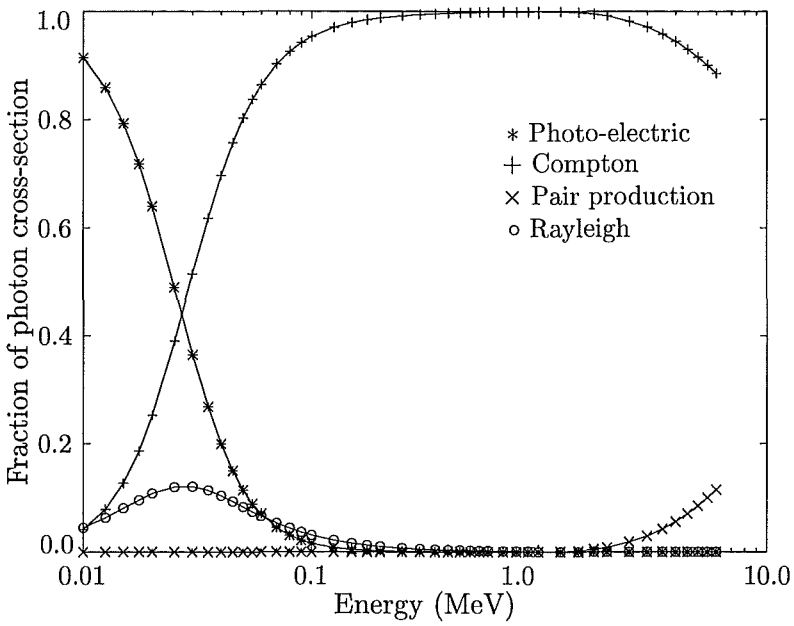

Figure 4.1: Relative importance of the various interactions which take place in water, as a function of incident photon energy. The Compton process is dominant in the energy range important for TBIDOS (50 keV to 6 MeV).

geneities (Johns and Cunningham, 1983).

Modern algorithms take these secondary electrons into account (Yu *et al*, 1995; Bortfeld *et al*, 1993). They also consider the effects on dose due to scattered photons from the Compton interaction. The first Compton scattered photon fluence is calculated from the Compton shift equation combined with the Klein-Nishina probability that a photon of energy E is scattered into a particular solid angle. Wong and Henkleman (1983) have shown for a cobalt-60 beam that multiple scattered photons account for 10% of the dose at a 15 cm depth. Techniques to include charged particle effects have been devised based on convoluting elementary dose distributions (kernels) with the primary dose distribution. ie. the primary dose distribution is convoluted spatially with the kinetic energy released at each site of primary photon-electron interaction. The kernels are calculated beforehand (Mackie *et al*, 1985) with Monte Carlo but must be modified for use in heterogeneous media (Ahnesjö, 1989).

The driving force behind the development of these codes has been to im-

prove the computation time for photon algorithms and much time and toil has been spent to achieve this by workers such as Bloch (1988), Brahme (1988), Boyer *et al* (1989) and Altschuler *et al* (1992). Their methods have many complexities and approximations especially when dealing with complex geometries (Knöös *et al*, 1995). The computing time for Monte Carlo is decreasing rapidly with modern CPU power. With the same approximations used as the algorithms (ie. no electron transport) the time needed will soon be short enough to enable routine use of Monte Carlo codes. Monte Carlo has the added advantage that electron transport and other realities can simply be 'switched on' for more realistic simulations and Monte Carlo inherently copes with complex geometries.

The Monte Carlo code was already installed on departmental computers so it was utilized for this work. The computers available were a few years old and relatively slow compared with recent machines. In hindsight photon algorithms should be installed and used since they are accurate enough for this work and would have saved much time. The experience gained using the Monte Carlo code was invaluable especially since its usage in medical physics is rapidly increasing.

4.2 Electron Gamma Shower simulation

The EGS4 code was developed at the Stanford Linear Accelerator Center by Nelson, Hirayama and Rogers. The basic photon transport algorithm used in this code is described below, further details may be found in the EGS4 manual (Nelson *et al*, 1985).

The modelling of a photon beam incident on the surface of a phantom or patient requires a large number of individual photons. When the photon enters the medium it will travel a certain distance before an interaction takes place. The average distance travelled depends on the medium, for a given photon energy this *mean free path*, λ, is given by

$$\lambda = \frac{M}{N_a \rho \sigma_t} \tag{4.2}$$

where

$$\begin{aligned} N_{\mathrm{a}} &= \text{Avogadro's number,} \\ \rho &= \text{density of the medium,} \\ M &= \text{molecular weight,} \\ \sigma_{\mathrm{t}} &= \text{total cross-section per molecule.} \end{aligned}$$

For an individual photon the number of mean free paths, N_λ, to the next interaction may be sampled by

$$N_\lambda = -\ln \zeta \tag{4.3}$$

with ζ being a random variable with a uniform distribution from 0 to 1. In any given situation there are many regions containing different media. Since the mean free path depends on the medium, the EGS4 code calculates the distance to the next interaction by summing over each medium along the particle's path accounting for the different values of λ in those regions.

At the interaction site, a number of events may take place including pair production, Compton scattering, the photo-electric effect and Rayleigh scattering. Other less significant interactions are Thomson scattering (important at low energies), nuclear photo-effect (12-24 MeV) and triplet production. The relative probability or 'branching ratios' of each event happening is well-known and is proportional to their cross-section. If the types of interaction are labelled 1 to n, with the jth interaction having cross-section σ_j, the branching ratios, $F(i)$ are given by

$$F(i) = \frac{1}{\sigma_t} \sum_{j=1}^{i} \sigma_j \tag{4.4}$$

where σ_t is the total cross-section. So by taking a uniform random variable on the interval $(0, 1)$ we may determine which interaction i takes place by finding $F(i)$ such that

$$F(i-1) < \zeta < F(i). \tag{4.5}$$

Now that the interaction location and type is known, the various attributes of the product particles are calculated. These parameters include scattering angles, calculated from the Klein-Nishina formulas in the case of Compton scattering and the approximate Beth-Heitler cross-section in the case of

pair-production (Bielajew, 1991). Photo-electrons are ejected in the same direction as the incoming photon in standard EGS4, but code has been distributed to give realistic electron angular distributions if needed for low energy work (Bielajew and Rogers, 1986). These approximations may be justified when the relative importance of each process is considered. For water, the relative cross sections verses photon energy are shown in figure 4.1. The Compton process clearly dominates in the range 50 keV to over 10 MeV and emphasises the relative unimportance of Rayleigh and pair production in this moderate energy range.

At each interaction point new particles may be produced, these particles are also transported through the media until discarded. A particle may be discarded by having an energy below some threshold or by leaving the region of interest. The user has control over both these criterion. During transport any energy transferred to the medium is tallied along with any other quantity which the user requires (type of interactions, scattering angles, spectra etc.). To use the EGS4 code system a routine called MAIN must be written. This sets up parameters used within the transport routines of EGS4. During the course of the simulation EGS4 eventually calls two user-written subroutines HOWFAR and AUSGAB. HOWFAR is called to determine the distance to the next medium boundary along the path of the particle. It is this subroutine which determines the geometry within the simulation and must be tested thoroughly to ensure particles are transported correctly. The subroutine AUSGAB is called when certain events occur like particle discards, this is where the dose is scored along with other parameters of interest.

4.3 TBIDOS geometry

The geometry of TBIDOS mimics the arc-TBI setup as described in chapter 3 with the definitions of figure 3.1. TBIDOS is based on a cartesian coordinate system with the origin at the isocentre, y-axis to the right, z-axis down and x-axis into the page as shown is figure 4.2. The water phantom consists of a rectangular volume bounded by planes $x = 0$, $x = 30$, $y = -50$, $y = 150$, $z = 50$ and $z = 80$ cm. These may be changed to any value by the user. The scoring volume is divided into volume elements (voxels) each of dimension 30 cm $\times$ 1 cm $\times$ 1 cm as shown in figure 4.2. These regions record the energy deposited within them, building up a dose map which is output as a matrix. The phantom is 30 cm wide in the x-direction to roughly approximate a patient.

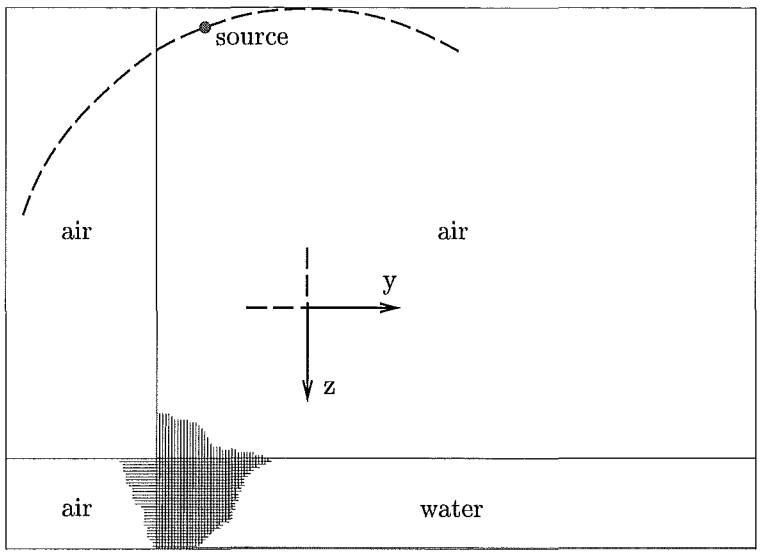

Figure 4.2: Geometry used in TBIDOS to model the arc-TBI treatment. The phantom is divided up into $30 \times 1 \times 1\,\mathrm{cm}^3$ regions in which the dose is scored. The output dose map consists of a matrix with elements corresponding to the squares in the water phantom.

The dose scored in these voxels represents the average along the width of the phantom.

The code works by injecting photons from the point source located on the arc in figure 4.2. The range of θ specified by the user is worked through sequentially as if the gantry is rotating about the isocentre. Each photon has an initial trajectory defined by θ and ϕ in the y-z plane and a random x-component to their trajectory which produces a fan-shaped beam slightly wider than the phantom. This mimics reality where the linac collimators are opened as wide as possible along the x-direction. The photons then travel through air towards the water phantom where most of the interactions occur. A small fraction exiting the far side without interacting are discarded along with the scattered photons exiting the geometry.

Each voxel is labelled by the indices i, j and k and are defined by the x, y and z planes which bound them. Given the three indices, the voxels may be labelled with a unique region number, IR. The subroutine HOWFAR written for TBIDOS checks to see which boundary is crossed when transporting a particle

and changes the current region number to represent the new voxel. Each region may be assigned a unique material, perhaps air to represent lung tissue or lead to mimic shielding. Keeping track of which region the particle occupies enables EGS4 to use the correct material cross-section data.

4.4 6 MV photons

Total body irradiation as proposed with the arcing technique uses a 6 MV photon beam produced by an isocentric linear accelerator. The beam is produced by accelerating electrons through a potential of 6 MV where they strike a thick tungsten target. The resulting bremsstrahlung radiation is collimated and filtered within the accelerator head and constitutes the *bremsstrahlung spectrum* or *primary spectrum.* Determining the spectrum of photon energies in this beam, and their variation with field position is a pressing problem in medical physics (Bissonnette and Schreiner, 1992; Carroll *et al*, 1993; Desobry and Boyer, 1994). This information determines the accuracy of treatment planning algorithms and Monte Carlo simulations alike (Zhu and Van Dyk, 1995).

Various methods are employed to determine spectra such as analytical calculations, transmission measurements, photo-activation analysis, Compton spectroscopy, depth dose reconstruction and Monte Carlo calculation. The first four methods have estimated uncertainties of 10-50% and are difficult to obtain (Williams, 1994). Using mono-energetic depth dose data to reconstruct spectra from experimental depth doses, and Monte Carlo simulation of the whole accelerator head are the most promising. An example of this is the code BEAM (Rogers *et al*, 1995), a general purpose Monte Carlo code which is capable of simulating the treatment head of any radiotherapy unit.

The energy spectrum used in TBIDOS is the 6 MV spectra calculated by (Mohan *et al*, 1985) and is shown in figure 4.3. A depth dose calculated with TBIDOS using this spectrum, with SSD = 150 cm and a beam width corresponding to a 10 cm by 10 cm field was compared to an ion chamber measured depth dose with the same SSD and field width. Although the two curves agree within 2% for all depths, this does not mean the spectra match as large variations in energy weightings produces similar depth dose curves. The important parameter which determines the depth dose is the mean energy in the spectrum (Mohan *et al*, 1985).

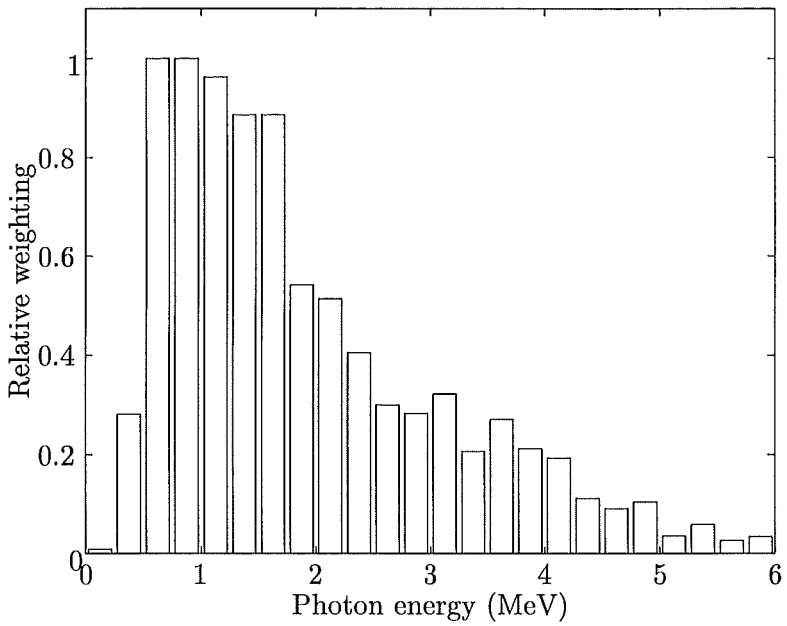

Figure 4.3: Photon energy spectrum for a 6 MV beam as calculated by Mohan *et al* (1985). This spectrum is used in all TBIDOS simulations.

4.5 Simulated material properties

The parameters for the material used in EGS4 are calculated prior to the program execution. Sets of data for each material used in the simulation are generated with the EGS4 preprocessor PEGS4. This program computes tables of the necessary cross-sections, mean free paths and stopping powers for each media. For each material the user is required to input the elemental makeup and density along with four other parameters; AE, AP, UE and UP. The first, AE, is the threshold energy for electron creation during Møller and Bhabha interactions. The second, AP, is the threshold energy for photon creation during the bremsstrahlung process. No particle below this energy is created. For example, when a secondary electron is produced with an energy below AE it will not be discretely transported, instead its energy is distributed according to a continuous energy loss model (Nelson *et al*, 1985). The other two parameters, UE and UP, represent the highest energy for which the material data is computed. In the TBIDOS water model the value used was AE = 0.521 MeV.

The photon threshold was set to AP = 0.010 MeV. The upper limits were set to UE = 6.511 MeV and UP = 6.0 MeV since 6.0 MeV is the highest photon energy used in these experiments and any photo-electron produced can not be higher than this. Having the range of energies matching those used in the simulation produces more accurate data sets compared to sets computed for a large energy range.

PIF (Prepare Input File) is an interactive program which runs through the necessary steps to produce the input file required by PEGS4. Elements, compounds or mixtures may be selected from a database of NIST compositions (Rogers *et al*, 1989) or the users own compositions may be used. Options such as Rayleigh scattering may be included and the density effect correction may be implemented from a database of Sternheimer-Seltzer-Berger coefficients. With the input file prepared, PEGS4 is called and the data sets are produced. The program EXAMIN may be run to inspect the dataset with graphs such as figure 4.1.

4.6 Sampling code

With the large amount of sampling required to transport a single particle and its shower products, the generation of random numbers is important. To better the statistics of measured values, a huge number of histories must be traced, 10^7 or more particles entering a system is not uncommon. The required large random number sets are supplied by 'pseudo' random number generators (RNGs) and provide the bedrock for Monte Carlo calculations (James, 1980).

A commonly used RNG and the default in standard EGS4 is Lehmer's method. This is a multiplication-linear-congruential method where a random number, ξ_i, may be generated from

$$\xi_i = (A\xi_{i-1} + B) \pmod{M} \tag{4.6}$$

where M is a modulus, A a multiplier and B is a constant. An initial seed ξ_0 must be supplied. The selection of the modulus depends on the computer architecture, in our case two lines of code are needed to give a random number R,

```
IXX = IXX * 663608941;
R = 0.5 + IXX * 0.23283064E - 09;
```

This RNG has a repetition cycle of $2^{30} \simeq 10^9$ which is adequate for about 10^6 electron histories. It should be noted that the seed value ξ_0 must be an odd number otherwise the cycle is reduced to the embarrassing value of one (due to the 32 bit computer architecture).

Fibonacci and shift register generators are considered better (James, 1990) since the set of random numbers has a cycle of $2^{570} \simeq 10^{171}$ and is machine independent. These Fibonacci sequences are produced by combining two preceding elements in some logic operation such that

$$\xi_i = (\xi_{i-p} \oplus \xi_{i-q}) \pmod{M} \tag{4.7}$$

where $\oplus$ is a binary or logical operation and p and q are the lags ($p > q$), giving the name *lagged Fibonacci sequence.* Of course the extra cycle length must be weighed against the added CPU time required to generate the sequence. In the case of TBIDOS the default RNG was used for initial testing and debugging of the program. The lagged Fibonacci sequence was later implemented because large numbers of particles were transported and the possibility of poor statistics was raised when using the default RNG. The lagged Fibonacci sequence took about 1.3 times longer to execute a given simulation.

The initial particle parameters required by EGS4 are the starting coordinates `XIN`, `YIN`, `ZIN`, direction cosines `UIN`, `VIN`, `WIN`, charge `IQIN`, initial region `IRIN`, and the initial energy `EIN`. The first parameter to be selected is linac position angle θ. The user specifies the linac output position and output modulation by specifying a file containing weighted angular divisions. A proportionate number of photons are started within each angular division to represent the required output. Given θ, `YIN` and `ZIN` are calculated for the source-isocentre distance of 1 m, `XIN` is set halfway between the two x-bounds. The initial trajectory is a function of θ and ϕ, where ϕ is a random angle constrained by the user-controlled beam width. The normalized direction cosines are then $\texttt{UIN} = \sin(\chi/2(\texttt{RNNO1} - 0.5))$, $\texttt{VIN} = \sin(\theta + \phi)$ and $\texttt{WIN} = \sqrt{1 - \texttt{UIN}^2 - \texttt{VIN}^2}$, where χ is the beam width angle in the x-direction. The charge is set to $\texttt{IQIN} = 0$ since all particles are photons. The initial region `IRIN` is calculated given the initial voxel indices `I`, `J`, `K`. The geometry is setup such that `I` is always 1 with `J` and `K` found by testing which boundaries `YIN` and `ZIN` fall between.

Selecting the initial energy `EIN` is slightly more difficult than the other parameters. The user must specify a file containing a probability distribution function (PDF) for an energy spectrum consisting of weighted energy bins. We

wish to sample an energy given a random number uniformly distributed over the range $(0, 1)$. This requires the PDF to be normalizable and non-negative. Firstly we construct its cumulative probability function (CDF) by summing the PDF components,

$$\mathrm{CDF}(E) = \sum_{i=E_{\min}}^{E} \mathrm{PDF}_i \tag{4.8}$$

and normalize

$$\mathrm{CDF}(E) = \frac{\mathrm{CDF}(E)}{\mathrm{CDF}(E_{\max})}. \tag{4.9}$$

This normalized CDF can then be mapped onto the range of random variables, ξ, where $0 \leq \xi \leq 1$.

The inverse CDF is then calculated to allow rapid sampling of the energy. An array `CDFINV` is computed which gives the energy as selected by a random number, along with the change in energy to the next bin. The input energy `EIN` is given by

$$\texttt{EIN} = \texttt{CDFINV}(\texttt{KK}, 1) + \texttt{CDFINV}(\texttt{KK}, 2) * \texttt{RNNO2} \tag{4.10}$$

where `KK` is the index selected from the random number and `RNNO2` is a second random number to ensure all energy ranges within a bin get sampled. The energy spectrum used in TBIDOS is from the file mohan6.spectrum shown in figure 4.3.

4.7 Validity of TBIDOS

The validity of the simulation depends on how well EGS4 models the physics of radiation transfer. Accuracy may be sacrificed for a shorter computing time by adjusting the parameters `ECUT` and `PCUT`.

`ECUT` and `PCUT` are the cutoff energies for electron and photon transport respectively. When the total energy of an electron (0.511 MeV + KE) falls below `ECUT`, transport stops, the particle is discarded and its kinetic energy is deposited in the current scoring region. Electron transport calculations are very time consuming due to the thousands of interactions an electron has before it comes to rest. These multiple collisions with the medium will be

Modelling	ECUT (MeV)	PCUT (MeV)	Relative time
High	0.521	0.010	1.00
Medium	1.311	0.010	0.09
Low	6.511	0.010	0.07

Table 4.1: Different radiation transfer parameters used to test the degree of modelling required by TBIDOS, with a comparison of the computation time.

modelled by a continuous energy loss when the electron energy is below the discrete interaction threshold AE. Another parameter ESTEPE represents the maximum fraction of energy lost during each electron step of the continuous loss transport. This parameter may be automatically chosen if the PRESTA routines are implemented (Bielajew and Rogers, 1987). These routines change the step size depending on how close the particle is to a boundary. In some complex geometries this will speed up the code. In TBIDOS the cutoff energy is always higher than the threshold energy so the transport is either discrete or non-existent and ESTEPE is somewhat redundant.

The values were chosen to minimize the code execution time whilst not compromising the physics involved. To confirm the effect of these approximations three depth doses were simulated with the beam normally incident upon the phantom ($\theta = 0°$). Each was calculated with different parameter values as listed in table 4.1 and correspond to high, medium and low physical reality. The first depth dose had accurate modelling with electrons transported until their kinetic energy was only 10 keV. The second had parameters where the electron cutoff was set to 1.311 MeV which means electrons with kinetic energies below 600 keV were not transported. This energy was chosen because an electron with 600 keV kinetic energy has a range (ICRU Report 35, 1984) of 0.33 cm or 1/3 the pixel size (1 cm $\times$ 1 cm) in TBIDOS. No change would be expected in the dose distribution in this case. The third depth dose had no electron transport and only transported photons. The photon transport was kept precise with PCUT = 0.010 MeV since a photon of this energy has a mean free path of 0.2 cm in water (Johns and Cunningham, 1983). The time saved by switching off the electron transport was enormous with only 7% of the time needed relative to the full transport. Stopping the transport of electrons with kinetic energies less than 600 keV caused a ten-fold decrease in CPU time. The

results showed that in the regions where CPE existed, at depths greater that 1.5 cm, all three curves agreed to within 1%. The difference was obvious in the buildup region where the effects of not transporting electrons were seen. The photon-only curve had maximum dose at the surface and decayed exponentially with depth, no buildup was measured. The other two curves were similar, showing the expected buildup curves but with a slightly higher (+5%) surface dose with medium modelling, caused by not transporting low energy electron to greater depths. Many investigations into the effect of changing parameters may be studied in Seltzer (1988).

The best option is to use a medium degree of modelling since this has quick execution times and predicts buildup curves quite accurately. Full electron transport may simply be switched on again if precise dose distributions are required in buildup regions or inhomogeneous regions.

Chapter 5

TBIDOS results

This chapter present results obtained by using the code TBIDOS. Various aspects of the arc-TBI treatment may be investigated with the code before performing the actual experiments. The effect of compensating the linac output with an inverse square relation is shown, along with depth compensating functions. The ability of this method to compensate around body contours is demonstrated. More conformal treatments may be simulated with an anthromorphic phantom, as shown at the end of this chapter.

5.1 Scoring dose

Whenever an event occurs during the particle shower, the subroutine AUSGAB is called by EGS4 with an argument which specifies the type of event. If a particle is being discarded its energy is added to the current region number associated with a particular voxel. This builds up a dose distribution within the water phantom modelled by TBIDOS.

The total number of histories N to be followed, is specified by the user and determines the statistical accuracy of the results (Bielajew, 1987). The number of histories may be split into n statistical batches of N/n particles each. The simulation is run for each of these n batches producing a dose matrix for each. The elements between each matrix are usually different due to the stochastic nature of the simulation. Since the corresponding element between batches has the value D_i, the mean value $\bar{D}$ is given by

$$\bar{D} = \frac{1}{n}\sum_{i=1}^{n} D_i \tag{5.1}$$

and the variance associated with the distribution of the D_i is

$$s_D^2 = \frac{1}{n-1}\sum_{i=1}^{n}(D_i - \bar{D})^2 \tag{5.2}$$

The estimated variance of $\bar{D}$ is

$$s_{\bar{D}}^2 = \frac{s_D^2}{n} \tag{5.3}$$

The dose in each voxel is then given by $D = \bar{D} \pm s_{\bar{D}}$. Most simulations are carried out using $n = 10$, with sufficient number of photons to give a 3% or better statistical variation of the dose between batches.

5.2 Constant output

The surface dose profile measured in a homogeneous phantom with a constant output approximately follows an inverse square fall-off, as shown by the measurements in figure 3.2. Figure 5.1 shows the dose distribution calculated with a constant output using TBIDOS. The surface dose of this distribution is shown in figure 5.1 obtained by plotting the mean dose deposited in the first and second rows of the dose matrix, these rows contain the depth of maximum dose ($z_{\max}$). The distribution was calculated with precise electron transport (ECUT = 0.521 MeV) since the surface region does not have charged particle equilibrium and the dose distribution due to electrons is important. It is thought that the Monte Carlo simulation agrees with the inverse square fall-off, and not with the measured values because no contaminant electrons are present in the simulation. These electrons originate from the linac collimator and cause a higher surface dose compared to uncontaminated photon beams (Johns and Cunningham, 1983). With a high angle of incidence the source-to-surface distance is much larger and these contaminant electrons do not reach the phantom, giving the lower measured surface dose at the phantom extremes (figure 3.2). The dominant effect is clearly the inverse square fall-off, at least for the surface. Compensating for this fall-off would be a good first step to a uniform dose and is investigated below.

5.3 Compensated output

As described in the previous chapter the controlled variation in output with gantry angle, $O(\theta)$, is specified with a file containing weighted angular bins (figure 5.6). Figure 5.2 shows the dose distribution obtained when the output is increased at the phantom extremities as the reciprocal of the the inverse square fall-off.

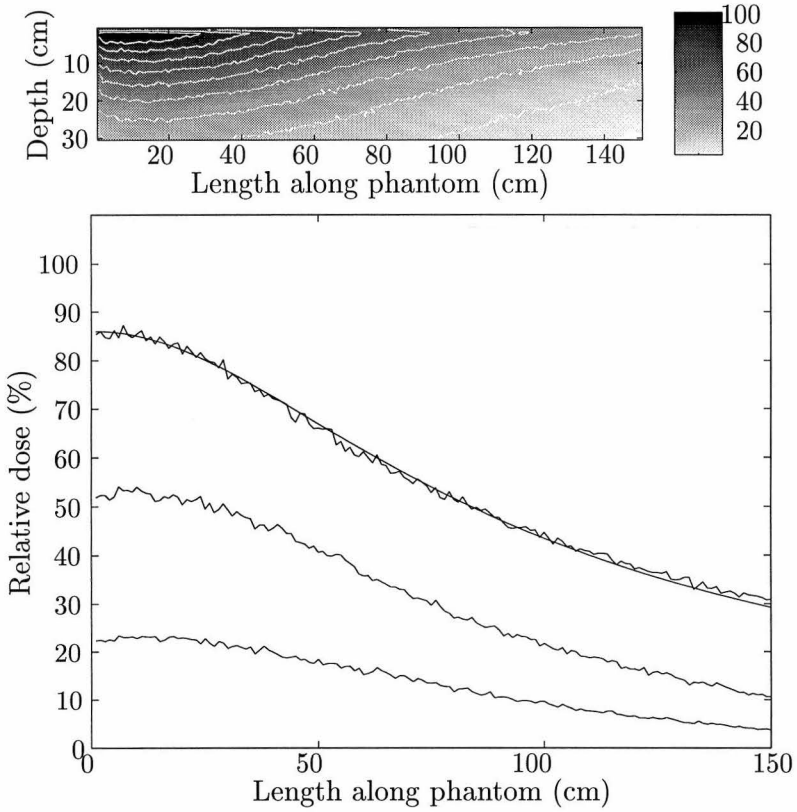

Figure 5.1: Dose distribution and isodose curves for a constant beam output with $f = 150\,\text{cm}$. The curves in the lower graph are dose profiles taken at the surface, midline and exit plane. The smooth curve is the expected inverse square fall-off at the surface.

The effect of this compensation is clear where it is seen that the surface dose has less variation. The slight increase in the surface dose towards the extremes is due to $z_{\max}$ being closer to the surface at these larger angles of incidence and is summed within the first scoring row. However the same figure immediately shows a problem in any thick target, namely that the midline dose ($z = 15\,\text{cm}$) of the phantom is far from uniform, ranging from 50% at $l = 0\,\text{cm}$ to about 20% at $l = 150\,\text{cm}$. This is caused by the extra material the beam passes through at large angles of incidence, producing a region of low dose where the patients feet may be located. With a prone/supine treatment the volume is given a more uniform dose. This is especially true for a 6 MV photon beam because

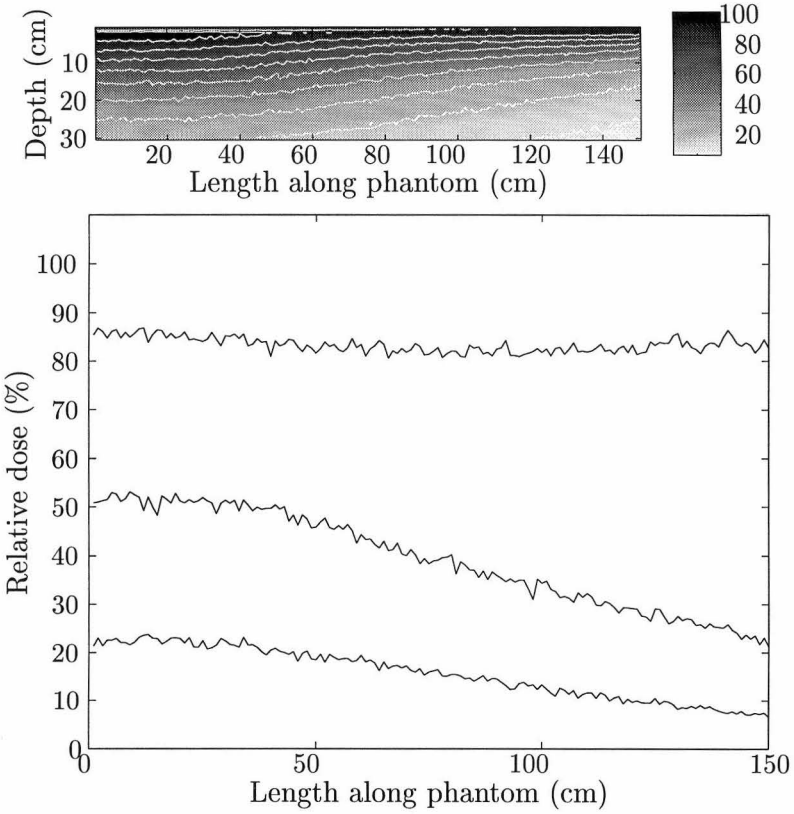

Figure 5.2: Dose distribution and isodose contours with output compensated by modulating the beam with the reciprocal of the inverse square falloff.

the half-value layer is 15 cm in water (Johns and Cunningham, 1983). This means the 50% dose point will roughly be at the same location when the beam is impinging from either direction. Figure 5.3 shows the dose distribution when this type of treatment is considered for a homogeneous phantom. The dose matrix was simply flipped in the vertical direction and added to the unflipped matrix mimicking a dose delivered in both the prone and supine positions.

The dose along the midline at a depth of 15 cm decreases markedly to a 50% level at 110 cm. This region of low dose at depth is due to the above photon attenuation caused by the added volume of water which the photons must traverse at these angles of incidence. This effect is exaggerated for a prone/supine treatment causing the dose at the extremes to be much lower. Figure 5.3 also shows the dose profile through the phantom at locations $l = 0$,

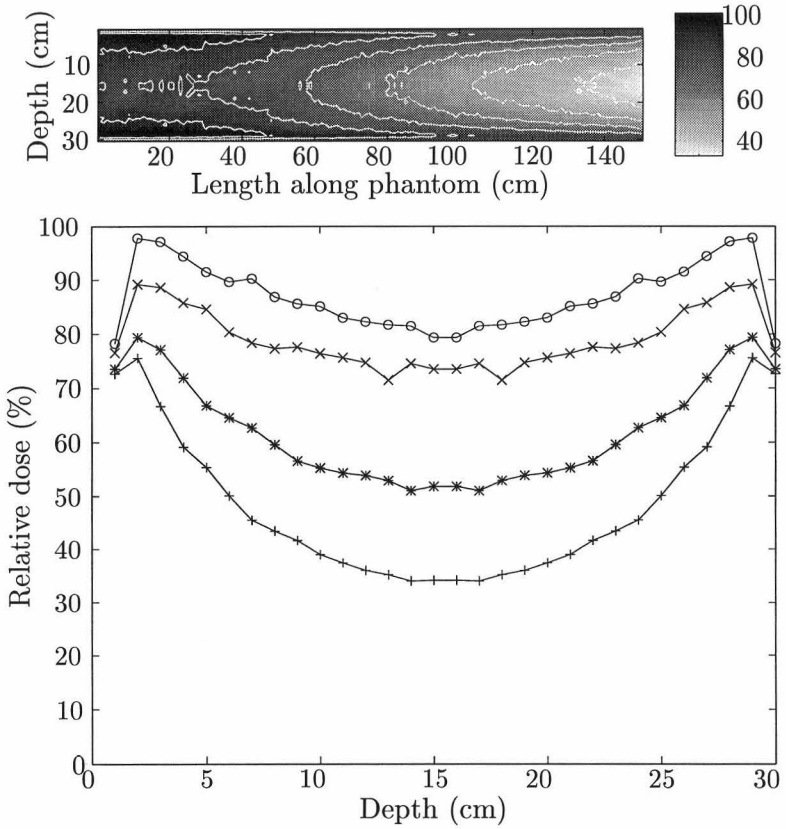

Figure 5.3: Dose distribution and isodose curves for a prone/supine treatment using an inverse square compensated beam output. The lower graph shows depth dose profiles at $l = 0\,\text{cm}$ (o), $l = 50\,\text{cm}$ (×), $l = 100\,\text{cm}$ (*) and $l = 150\,\text{cm}$ (+).

50, 100, 150 cm. The profiles have variations of 15% at $l = 0\,\text{cm}$ to 40% at $l = 150\,\text{cm}$. This is obviously unsatisfactory for a real treatment and adjustments to the linac output would be necessary to reduce this variation to acceptable levels. Increasing the output further at high angles of incidence will help correct the low dose at the phantom extremes but this will cause a high surface dose. This high surface dose is offset somewhat by using a prone/supine treatment because the dose will be averaged with the very low exit dose at these locations. A slight improvement may be achieved if the inverse square compensation is replaced by another output function designed to deliver a uniform dose to the midline at $z = 15\,\text{cm}$. This was derived by using the reciprocal of the

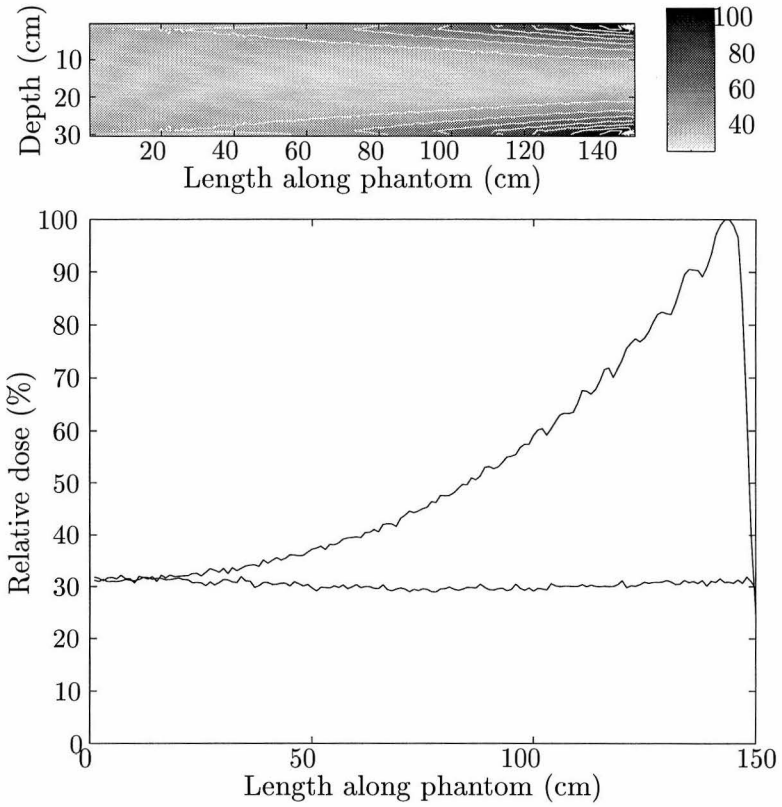

Figure 5.4: Prone/supine dose distribution and isodose curves showing the flat midline dose. This was achieved by considering the expected photon attenuation at depth in water. The lower graph shows the uniform midline dose distribution (lower curve) at the expense of a high surface dose (upper curve).

expected midline dose. The expected dose takes two effects into account, the inverse square fall-off and the photon attenuation in the water. The output modulation is then $O(\theta) = M(\theta)^{-1}$ with

$$M(\theta) = \frac{165^2}{(100 + 65/\cos\theta)^2} e^{-x/\lambda} \tag{5.4}$$

where $x = 15/\cos\theta$ cm is the thickness of water traversed at various angles and $\lambda = 17\,\mathrm{cm}^{-1}$ is the mean free path for a 6 MV photon beam in water (Johns and Cunningham, 1983). At large angles of incidence the output is very high, resulting in a similarly high surface dose. With a prone/supine treatment

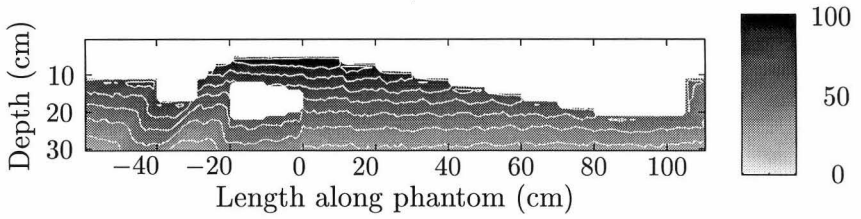

Figure 5.5: Dose distribution and isodose curves within an anthropomorphic phantom subjected to an inverse square modified beam. This image highlights the dose inhomogeneities about the neck and lung regions.

this will be averaged with the opposing beam's low exit dose, reducing the effect. The midline dose is extremely flat but figure 5.4 shows how the surface dose is affected, being three times higher than the midline. This high dose is due to compensating in regions beyond the phantom, a discontinuous output function may be devised to solve the problem. Nevertheless, this demonstrates the ability to control the profile at depth, simply by adjusting the output modulation correctly.

5.4 Anthropomorphic phantoms

The TBIDOS code is general enough to specify any shape made from any material and see the dose distribution when subjected to the arc-TBI treatment. The object must be composed of rectilinear voxels. The voxels may be very small but large numbers will slow the execution time of the code. An anthropomorphic phantom was created to examine the dose distribution with a more realistic patient shape compared to the homogeneous phantom. The shape consisted of a head, neck, torso, legs and feet. Lung were included also which consisted of an isolated volume of air of similar shape and size to the real thing. Figure 5.5 shows the dose distribution within the phantom after being irradiated with an inverse square modified beam. The dose distribution was surprisingly homogeneous, with the shape of the phantom helping to give more uniform dose profiles. The problems of increased dose about the neck and lung areas is obvious with the dose at $z = 25\,\text{cm}$ some 15% higher. These inhomogeneities need to be accounted for when delivering dose to patients. This is where the output modulation abilities of the arc-TBI technique are

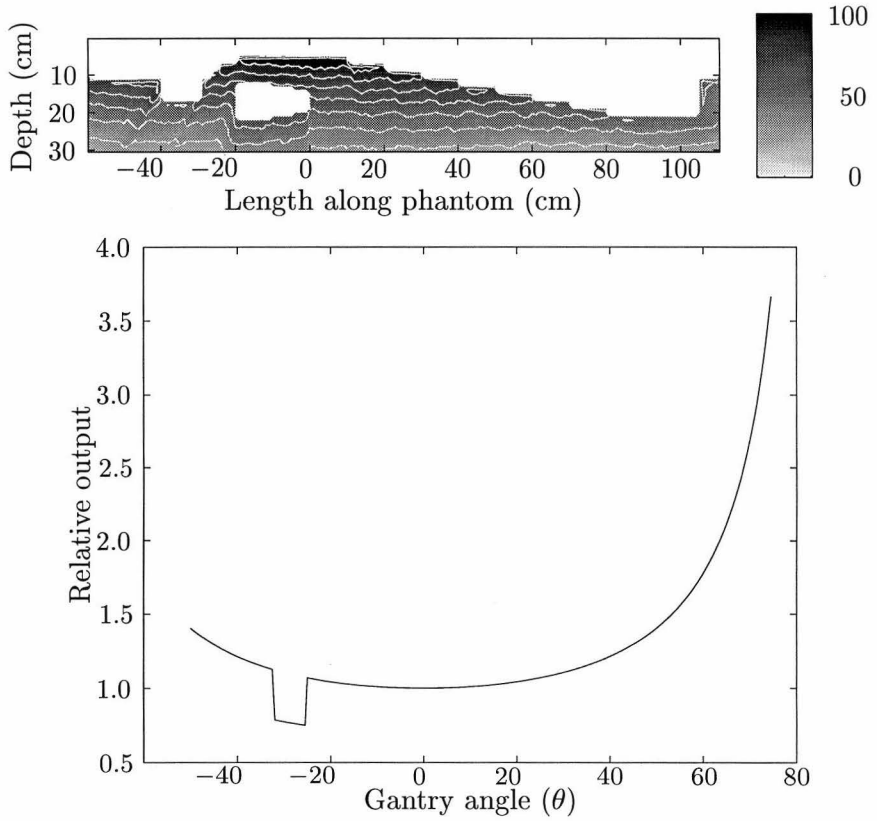

Figure 5.6: Dose distribution and isodose curves within an anthropomorphic phantom using the output function in the lower graph. This output function is decreased in the neck region to produce the flatter neck profile.

useful. The location of the neck area lies between the angles $\theta = -32°$ and $\theta = -25°$. The output dose was modified over this range to account for the lack of water attenuation. There was approximately one mean free path less water along the path so the output was reduced to 70% between these angles. The modified dose profile is shown in figure 5.6. The dose about the neck now matches other regions at similar depths. When combined with a prone treatment the dose should remain uniform throughout the phantom.

A prone/supine treatment was trialed using the anthropomorphic phantom. Two different output functions were used. The depth modified inverse square which gave the dose distribution in figure 5.4 was used for the prone treatment.

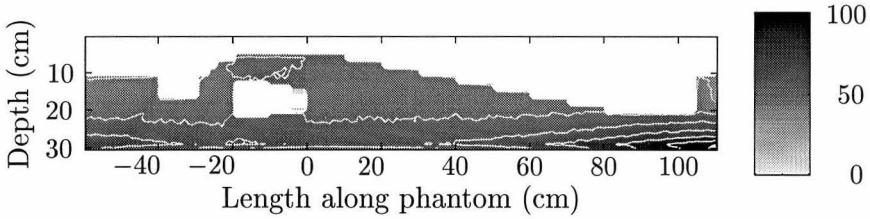

Figure 5.7: Dose distribution and isodose curves within an anthropomorphic phantom which was subjected to a prone/supine treatment. This image highlights the dose uniformity and the effect of the high surface dose at extreme location.

This gives a flat dose profile through the midline. The neck-compensated output function was used for the supine treatment as this gave flat midline in the supine position. Each matrix was normalized at the midline to represent equivalent doses. They were then added together to form the image in figure 5.7. The high dose at the phantom's feet may be decreased with a discontinuous beam output. The lung was not compensated, giving the slightly higher dose above and below. The large homogeneous region shows the arc-TBI technique can successfully deliver uniform dose to a patient-like volume.

Chapter 6

Conclusions

The code written for this thesis, TBIDOS, may be continually improved. A full three-dimensional anthropomorphic phantom may be implemented to study the dose profile along the width of the patient. Internal organs and bone may be incorporated to observe how they perturb the photon beam. They are not currently implemented because the added computation time is not justified. In its present state the code is capable of modelling any phantom shape and internal structure. The grid size may be increased to lower computing times or decreased to produce smooth detailed contours within the phantom. The code may use any output function to modify the beam intensity. It was observed that small changes in output have a noticeable effect on the dose profile. For this reason the code is useful in fine-tuning the desired output function before the time-consuming experimental measurements are made.

The results presented in chapter 5 show how various compensation functions perform. The best option was found to be an inverse square relation combined with a photon attenuation term. This gave a very flat profile through the phantom midline. Consequently there was a high surface dose but this may be controlled with further output modulation. The technique's ability to compensate for patient anatomy was demonstrated by correcting the dose profile about the neck. The large homogeneous regions within the anthropomorphic phantom is testament to the technique's success. At the short source-to-surface distance involved (150 cm) the patient may lie on the existing couch. This benefit is enormous, as the routine may become part of other day-to-day treatments within many oncology centres. To establish a clinical treatment a few standard body shapes should be defined. Then the effect of different output functions should be examined on each. The dependence on body shape will determine how many different output functions are needed to treat all patients. The next step in this work would involve taking measurements in a real phantom. Once the linac control software is available, this will be possible. The results may then be published in a referred journal as part

II following Hugtenburg *et al.* The simulations enable the optimum output function to be found before the experiments take place.

Chapter 2 described the production and testing of an *in vivo* sarcomere length measuring instrument. The instrument was based on the concept of Lieber and Baskin (1985). Several operations were attended to trial different versions of the instrument. A diode laser was tried but coherence problems required a change to a He-Ne gas laser. Several glass rods were ground, polished and tested. They were satisfactory but much better results were obtained with a square rod professionally polished. The final version uses a He-Ne gas laser, square glass rod with a calibrated screen. This enables the surgeon to directly measure sarcomere length with a 3% precision. Results of clinical trials, which use this instrument to find the optimum sarcomere length, may be published. This will improve tendon transfer techniques and help the patient's recovery.

Acknowledgements

I would like to thank my three official supervisors who were involved in these two projects. Thanks to Associate Professor Philip Butler at the University of Canterbury for his suggestions regarding the sarcomere instrument and for his editorial input. Professor Alastair Rothwell at the Department of Orthopaedic Surgery and Musculoskeletal Medicine, Christchurch Hospital, provided the opportunity to attend several fascinating operations. Thanks to John Turner at the Christchurch Hospital Oncology Service for making the arc-TBI project available and allowing access to the hospital resources.

Many thanks to Richard Hugtenburg, a Ph.D. candidate at the University of Canterbury. Richard was extremely helpful explaining the complexities of EGS4. His help operating the linac and pointing out bugs in TBIDOS is also appreciated.

I would like to thank the technicians from the department who helped with the sarcomere instrument. Especially Wayne Smith who built the various mounts used in the design. Also Graeme Kershaw, Stephen Hemmingsen, and Robert Thirkettle who helped with other aspects of the instrument.

References

Ahnesjö A 1989 Collapsed cone convolution of radiation energy for photon dose calculation *Med. Phys.* **16** 577–591

Altringham J D, Bottinelli R, and Lacktis J W 1984 Is stepwise shortening an artefact? *Nature* **307** 653–655

Altschuler M D, Bloch P, Buhle E L J, and Ayyalasomayajula S 1992 3-d dose calulations for electron and photon beams *Phys. Med Biol.* **37** 391–441

Astrahan M A, Luxton G, Jozsef G, Kampp T D, Liggett P E, Sapozink M D, and Petrovich Z 1990 An interactive treatment planning system for opthalmic plaque radiotherapy *Int. J. Radiation Oncology Biol. Phys.* **18** 679–687

Baskin R J, Lieber R L, Oba T, and Yeh Y 1981 Intensity of light diffraction from striated muscle as a function of incident angle *Biophys. J.* **36** 759–773

Bielajew A F and Rogers D W O 1986 *Photoelectron angular distribution in the EGS4 code system* National Research Council of Canada Report: PIRS-0058

——— 1987 Presta: The parameter reduced electron-step transport algorithm for electron monte carlo transport *Nucl. Instrum. Meth.* **B 18** 165–181

Bielajew A F 1987 *Efficiency, statistics, and sampling* National Research Council of Canada Report: PIRS-0395

——— 1991 *Improved angular sampling for pair production in the EGS4 code system* National Research Council of Canada Report: PIRS-0287

Bissonnette J and Schreiner L J 1992 A comparison of semiempirical models for generating tungsten target x-ray spectra *Med. Phys.* **19** 579–582

Bloch P 1988 A unified electron/photon dosimetry approach *Phys. Med. Biol.* **33** 373–379

Bortfeld T, Schlegel W, and Rhein B 1993 Decomposition of pencil beam kernels for fast dose calculations in three-dimensional treatment planning *Med. Phys.* **20** 311–318

Boyer A L, Zhu Y, Wang L, and Francois P 1989 Fast fourier transform convolution calculations of x-ray isodose distributions in homogeneous media *Med. Phys.* **16** 248–253

Brahme A 1988 Optimization of stationary and moving beam radiation therapy techniques *Radiother. Oncol.* **12** 129–140

Buchthal F and Knappeis G G 1940 Diffraction spectra and minute structure of the cross-striated muscle fibre *Skand. Arch. Physiol.* **83** 281

Burton K and Huxley A F 1995 Identification of source oscillations in apparent sarcomere length measured by laser diffraction *Biophys. J.* **168** 2429–2443

Carroll J J, Richmond T W, Sinor T W, Taylor K N, Hong C, Standifird J D, and Collins C B 1993 Absolute measurement of spatial and spectral characteristics of bremsstrahlung using the photoexcitation of nuclear isomers *Rev. Sci. Instrum.* **64** 2298–2305

Desobry G E and Boyer A L 1994 An analytic calculation of the energy fluence spectrum of a linear accelerator *Med. Phys.* **21** 1943–1952

Fleeter T B, Adams J P, Brenner B, and Podolsky R J 1985 Laser diffraction, application to tendon transfers *J. Hand Surg.* **10A** 542–546

Glascow G P and Mill W B 1980 Cobalt-60 total body irradiation dosimetry at 220 cm source-axis distance *Int. J. Radiation Oncology Biol. Phys.* **6** 773–777

Hugtenburg R P, Turner J R, Baggarley S P, Pinchin D A, Oien N A, Atkinson C H, and Tremewan R N 1994 Total-body irradiation on an isocentric linear accelerator *Phys. Med. Biol.* **39** 783–793

Huxley H and Hanson J 1954 Changes in the cross-striations of muscle during contraction and stretch and their structural interpretation *Nature* **173** 973–976

Huxley A F and Niedergerke R 1954 Structural changes in muscle during contraction *Nature* **173** 971–973

Huxley A F 1990 A theoretical treatment of diffraction of light by a striated muscle fibre *Proc. R. Soc. Lond. B* **241** 65–71

ICRU Report 35 1984 *Radiation Dosimetry: Electron beams with energies between 1 and 50 MeV* ICRU, Washington DC

Jackson J D 1975 *Classical Electrodynamics* (John Wiley & Sons, Inc) Second edition

James F 1980 Monte Carlo theory and practice *Rep. Prog. Phys.* **43** 1145–1189

——— 1990 A review of pseudorandom number generators *Computer Physics Communications* **60** 329–344

Johns H E and Cunningham J R 1983 *The physics of radiology* (Thomas, Illinois) Forth edition

Kawai M and Kuntz I D 1973 Optical diffraction studies of muscle fibers *Biophys. J.* **13** 857–876

Kim T H, Khan F M, and Galvin J M 1980 A report of the work party: Comparison of total body irradiation techniques for bone marrow transplantation *Int. J. Radiation Oncology Biol. Phys.* **6** 779–784

Knöös T, Ahnesjö A, Nilsson P, and Weber L 1995 Limitations of a pencil beam approach to photon dose calculations in lung tissue *Phys. Med. Biol.* **40** 1411–1420

Lieber R L and Baskin R J 1985 *Surgical myometer method* U.S. Patent Number 4,570,641

Lieber R L, Yeh Y, and Baskin R J 1984 Sarcomere length determination using laser diffraction *Biophys. J.* **45** 1007–1016

Mackie T R, Scrimger J W, and Battita J J 1985 A convolution method of calculating dose for 15 mv x-rays *Med. Phys.* **12** 188–196

Mohan R, Chui C, and Lidofsky L 1985 Energy and angular distributions of photons from medical linear accelerators *Med. Phys.* **12** 592–597

Nelson W R, Hirayama H, and Rogers D W O 1985 *The EGS4 code system* Stanford Linear Accelerator Center SLAC-Report-265

Paolini P J, Sabbandini R, Roos K P, and Baskin R J 1976 Sarcomere length dispersion in single skeletal muscle fibers and fiber bundles *Biophys. J.* **16** 919–930

Pla M, Chenery S G, and Podgorsak E B 1983 Total body irradiation with a sweeping beam *Int. J. Radiation Oncology Biol. Phys.* **9** 83–89

Quast U 1985 Physical treatment planning of total-body irradiation: Patient translation and beam-zone method *Med. Phys.* **12** 567–574

Rogers D W O, Duane S, Bielajew A F, and Nelson W R 1989 *Use of ICRU-37/NBS radiative stopping powers in the EGS4 system* National Research Council of Canada Report: PIRS-0177

Rogers D W O, Faddegon B A, Ding G X, Ma C M, Wei J, and Mackie T R 1995 Beam: A Monte Carlo code to simulate radiotherapy treatment units *Med. Phys.* **22** 503–524

Rüdel R and Zite-Ferenczy F 1979 Interpretation of laser diffraction by cross-striated muscle as Bragg reflexion of light by the lattice of contractile proteins *J. Physiol.* **290** 317–330

Salmons S, editor 1995 *Gray's Anatomy* (Churchill Livingstone, New York, N.Y.) Thirty-eighth edition

Sandow A 1936 Diffraction patterns of the frog sartorius and sarcomere behaviour under stretch *J. Cell Compar. Physiol.* **9** 37–54

Seltzer S M 1988 An overview of ETRAN Monte Carlo methods in *Monte Carlo transport of electrons and photons* , edited by Jenkins T M, Nelson W R, and Rindi A chap 7, pages 153–181 (Plenum Publishing Corporation)

Sidick E, Knoesen A, Xian J K, Yeh Y, and Baskin R J 1992 Rigorous analysis of light diffraction by a striated muscle fibre *Proc. R. Soc. Lond. B* **249** 247–257

Thornhill R A, Thomas N, and Berovic N 1991 Optical diffraction by well-ordered muscle fibres *Eur. Biophys. J.* **20** 87–99

Van Dyk J, Battista J J, and Rider W D 1980 Half body radiotherapy: The use of computed tomography to determine the dose to lung *Int. J. Radiation Oncology Biol. Phys.* **6** 463–470

Williams J 1994 *Megavoltage bremsstrahlung spectra from therapeutic linear accelerators* Honours project, University of Canterbury

Wilson R R 1952 Monte Carlo study of shower production *Phys. Rev.* **86** 261

Wong J W and Henkleman R M 1983 A new approach to CT-pixel-based photon dose calculations in hetrogeneous media *Med. Phys.* **10** 199–208

Yeh Y, Baskin R J, Lieber R L, and Roos K P 1980 Theory of light diffraction by single skeletal muscle fibers *Biophys. J.* **29** 509–522

Yu C X, Mackie T R, and Wong J W 1995 Photon dose calculation incorporating explicit electron transport *Med. Phys.* **22** 1157–1165

Zhu Y and Van Dyk J 1995 Accuracy requirements of the primary x-ray spectrum in dose calculations using FFT convolution techniques *Med. Phys.* **22** 421–426